PAPER

Check for updates

Surface reaction kinetics of the methanol synthesis and the water gas shift reaction on Cu/ZnO/Al$_2$O$_3$†

Bruno Lacerda de Oliveira Campos, [iD] [a] Karla Herrera Delgado, [iD] *[a] Stefan Wild, [iD] [a] Felix Studt, [iD] [ab] Stephan Pitter [iD] [a] and Jörg Sauer [iD] [a]

A three-site mean-field extended microkinetic model was developed based on *ab initio* DFT calculations from the literature, in order to simulate the conversion of syngas (H$_2$/CO/CO$_2$) to methanol on Cu (211) and Cu/Zn (211). The reaction network consists of 25 reversible reactions, including CO and CO$_2$ hydrogenation to methanol and the water-gas shift reaction. Catalyst structural changes are also considered in the model. Experiments were performed in a plug flow reactor on Cu/ZnO/Al$_2$O$_3$ at various gas hourly space velocities (24–40 L h^{-1} g$_{cat}^{-1}$), temperatures (210–260 °C), pressures (40–60 bar), hydrogen feed concentrations (35–60% v/v), CO feed concentrations (3–30% v/v), and CO$_2$ feed concentrations (0–20% v/v). These experiments, together with experimental data from the literature, were used for a broad validation of the model (a total of 690 points), which adequately reproduced the measurements. A degree of rate control analysis showed that the hydrogenation of formic acid is the major rate controlling step, and formate is the most sensitive surface species. The developed model contributes to the understanding of the reaction kinetics, and should be applicable for industrial processes (*e.g.* scale-up and optimization).

1 Introduction

Methanol is a viable high-value energy carrier and a key intermediate in the chemical industry, as it can be used in many energy and chemical production applications.[1,2] Methanol is synthesized from syngas (H$_2$/CO/CO$_2$), which is industrially produced from natural gas and coal.[3] However, because of concerns regarding CO$_2$ emissions and encouragements to the development of sustainable processes using renewable energy sources, alternatives to the generation of syngas are in the focus of worldwide research. Promising approaches include the gasification of biomass[4,5] and the use of green electricity (*e.g.* from solar and wind power) to generate hydrogen *via* water electrolysis,[6] further mixing it with carbon dioxide (*e.g.* from the flue gas of a process).[7] Thereby, the importance of the methanol synthesis will increase, as the conversion of hydrogen to secondary energy carriers is crucial.[8] A scheme with the mentioned process steps is shown in Fig. 1.

[a] *Institute for Catalysis Research and Technology (IKFT), Karlsruhe Institute of Technology (KIT), Hermann-von-Helmholtz-Platz 1, 76344 Eggenstein-Leopoldshafen, Germany. E-mail: karla.herrera@kit.edu; Tel: +49 721 608 28631*
[b] *Institute for Chemical Technology and Polymer Chemistry (ITCP), Karlsruhe Institute of Technology (KIT), Engesserstr. 18-20, 76131 Karlsruhe, Germany*
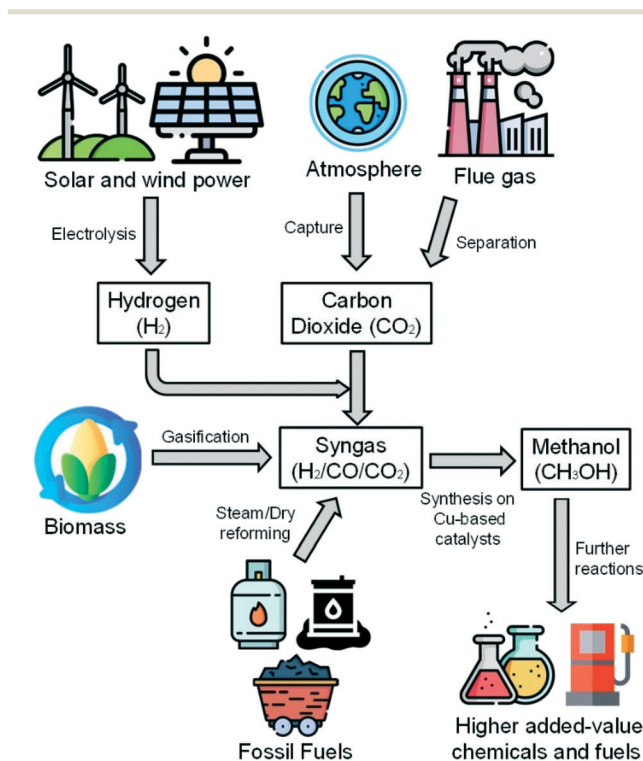† Electronic supplementary information (ESI) available. See DOI: 10.1039/d1re00040c
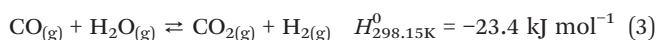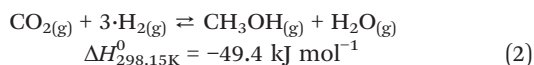
Fig. 1 From syngas sources to higher added-value chemicals and fuels *via* methanol synthesis. Images: Freepik, Flaticon.[10]

868 | *React. Chem. Eng.*, 2021, **6**, 868–887

This journal is © The Royal Society of Chemistry 2021

Typically, industrial methanol production takes place in continuous processes using copper-based catalysts (e.g. Cu/ZnO/Al$_2$O$_3$) at 50–100 bar and 200–300 °C.[9]

Three main reactions occur: CO hydrogenation (eqn (1)), CO$_2$ hydrogenation (eqn (2)) and the water-gas shift reaction (WGSR) (eqn (3)).

$$CO_{(g)} + 2 \cdot H_{2(g)} \rightleftharpoons CH_3OH_{(g)} \quad \Delta H^0_{298.15K} = -90.6 \text{ kJ mol}^{-1} \quad (1)$$

$$CO_{2(g)} + 3 \cdot H_{2(g)} \rightleftharpoons CH_3OH_{(g)} + H_2O_{(g)}$$
$$\Delta H^0_{298.15K} = -49.4 \text{ kJ mol}^{-1} \quad (2)$$

$$CO_{(g)} + H_2O_{(g)} \rightleftharpoons CO_{2(g)} + H_{2(g)} \quad H^0_{298.15K} = -23.4 \text{ kJ mol}^{-1} \quad (3)$$

Several kinetic models have been developed to simulate the methanol synthesis.[11–16] Graaf et al.[11] proposed a model considering the three global reactions (eqn (1)–(3)), one active site for CO and CO$_2$ adsorption and one for H$_2$ and H$_2$O adsorption. Vanden Bussche and Froment[12] proposed a model considering CO$_2$ as the main carbon source of methanol and neglecting CO hydrogenation, but maintained the same active sites as Graaf et al.[11] Ovesen et al.[13] considered the three global reactions (eqn (1)–(3)), one active site for CO adsorption and another one for CO$_2$ adsorption, and proposed structural changes in the catalyst active sites depending on the gas composition. Park et al.[14] considered the three global reactions (eqn (1)–(3)) and three active sites (for CO adsorption, for CO$_2$ adsorption, and for H$_2$/H$_2$O adsorption). Seidel et al.[15] considered all three reactions and three active sites, applying the structural changes proposed by Ovesen et al.[13] as well. In a recent work, Slotboom et al.[16] proposed a model with a reduced amount of parameters (6) to decrease identifiability problems. In their approach, CO hydrogenation (eqn (1)) was neglected, and three active sites were considered.

Although each model has its particular considerations, they all have rate determining steps (RDS) assumptions, which means that groups of parameters are lumped and fitted to experimental data. With this method, different effects may be merged with kinetics and cause the models to diverge outside the training region, which is often narrow.

Microkinetic modeling takes into account the chemistry behind the process,[17] being useful for better understanding of the system, for process optimization and for catalyst development. Based on data derived from first principles density functional theory (DFT) during the last decade, detailed microkinetic models have been proposed for methanol synthesis,[18–23] in which different surface reaction paths are considered and all reactions are potentially rate limiting. Grabow and Mavrikakis[18] proposed a mechanism for CO/CO$_2$ hydrogenation and the WGSR on Cu (111). In the adsorption steps, sticking coefficients equal to one were considered. The authors concluded that a more open surface (e.g. Cu (110), Cu (100), Cu (211)) could better represent the catalyst active area, and that the synergic effect of ZnO has to be taken into account, both conclusions being later

demonstrated by Behrens et al.[24] Van Rensburg et al.[19] used previously reported DFT data[24,25] to test microkinetic mechanisms for CO and CO$_2$ hydrogenation on different surfaces (Cu (111), Cu (211), and Cu/Zn (211)), without including a mechanism for the WGSR. Liu et al.[20] compared the mechanisms on Cu$_2$O (111) and on Cu (111), and concluded that CO hydrogenation is faster on Cu$_2$O, whereas CO$_2$ hydrogenation is the dominating path on Cu (111). Park et al.[21] proposed a mechanism on Cu (211), in which adsorption and activation energies were taken from DFT-derived data, and pre-exponential factors were fitted to experimental data. Xu et al.[22] proposed a mechanism on Cu (211) and compared three situations: clean surface, preadsorbed O*, and preadsorbed OH*. The conclusion was that the preadsorbed species create faster reaction paths for the hydrogenation of formate. Huš et al.[23] developed a mechanism on Cu (111) for different metal oxides (Zn$_3$O$_3$, Cr$_3$O$_3$, Fe$_3$O$_3$, Mg$_3$O$_3$) combined with copper, and concluded that the Zn$_3$O$_3$/Cu system has a superior performance.

In the aforementioned DFT-based models, single active sites were considered, and thus no structural changes in the catalyst were mentioned, despite being well known that Cu-based catalysts suffer morphology changes depending on gas composition and temperature, affecting the catalyst activity.[26–29] To the best of our knowledge, only Huš et al.[23] validated their model with own experimental data. The other models cited above were either validated with experiments reported in literature,[11] or there was no validation at all.

Summarizing the modeling studies for methanol synthesis in the literature, to our knowledge, yet no published kinetic model exists that accounts for all these key features in methanol synthesis on Cu/ZnO/Al$_2$O$_3$:

• The global mechanism considers reactions (1)–(3).

• All surface reactions are potentially rate limiting (detailed microkinetic approach).

• The facet of Cu (211), a more open and active surface of the catalyst, is considered.

• Three-site approach: besides the Cu (211) active site (site a), the synergy of zinc is taken into account with the assumption of a Cu/Zn or Cu/Zn$^{\delta+}$ (211) active center (site b), and a separate site is considered for the adsorption of H$_2$ and H$_2$O (site c) to avoid the adsorption inhibition caused by formate.

• The structural changes of the catalyst, which are dependent on temperature and gas phase composition variations, are quantitatively taken into account.

• An extensive experimental validation is made covering the most important parameters in methanol synthesis: pressure, temperature, gas hourly space velocity (GHSV), and the feed composition (H$_2$, CO and CO$_2$).

In this work, a multiscale kinetic model for the methanol synthesis and the WGSR is presented, in which all these aspects are considered. A wide experimental validation shall allow for simulating the methanol synthesis at different operating conditions.

2 Experimental setup

A total of 359 experiments were conducted in a single fixed-bed plug flow reactor (PFR). The operating conditions were varied in terms of temperature (210–260 °C), pressure (40–60 bar), gas hourly space velocity (GHSV) (24–40 L h^{-1} g$_{cat.}^{-1}$), hydrogen feed concentration (35–60% v/v), CO feed concentration (3–30% v/v), and CO_2 feed concentration (0–20% v/v). Full experimental data are provided in the ESI† (Table S1).

The PFR set-up consisted of a stainless steel tube with 460 mm length, an inner diameter of 12 mm, and an inner concentric tube (2 mm) for temperature measurements in the axial direction. The feed gases were hydrogen (99.999% v/v), carbon monoxide (99.97% v/v), nitrogen (99.9999% v/v), and a mixture of carbon dioxide and nitrogen (50 : 50 ± 1.0% v/v) (Air Liquide Germany GmbH). The reactant gases supply was regulated *via* mass flow controllers (MFCs, Bronkhorst High Tech), by using proportional-integral-derivative (PID) control. The MFCs were calibrated with a flowmeter (Defender 530+, Mesalabs, standard error: 1.0% v/v). Both reactants (*via* bypass) and products were analyzed with a Fourier transform infrared spectrometer (FTIR, Gasmet CX4000). A flow diagram of the experimental setup is shown in Fig. S1.†

The reactor was filled with a commercial CuO/ZnO/Al$_2$O$_3$ catalyst provided by an industrial partner, which was crushed and sieved to a particle size range between 250 and 500 μm. As the methanol synthesis is exothermic, and in order to avoid hot spots and to ensure isothermal operation, five portions of 0.30 g catalyst (in total 1.50 g), were separately mixed, each with 8.18 g of silicon carbide (SiC, Hausen Mineraliengroßhandel GmbH) (in total 40.90 g). Each mixture was then consecutively filled into the reactor, forming a catalytic bed length of 200 mm. Pure SiC completed the upper and lower ends of the bed.

The catalyst was activated as follows: a volume flow of 300 mL$_S$ min^{-1} containing 5% v/v of H$_2$ in N$_2$ was applied to the reactor, and the system was heated from 100 to 200 °C at a heating rate of 20 °C h^{-1}. This temperature was hold for one hour, followed by further heating to 240 °C at a heating rate of 12 °C h^{-1}. Finally, the H$_2$ concentration in the flow was increased to 50% v/v, maintaining the same total flow rate for one more hour.

In order to obtain a stable catalyst in steady-state conditions, the reactor was operated for 320 h at 40 bar, different temperatures (210–260 °C), and different feed gas compositions, before starting the measurements reported here.

The temperature axial profile was measured using a type-K thermocouple (NiCr–Ni) for the two data points with the highest methanol productivity, and thus the highest energy release due to the exothermic reactions. Since the maximum temperature difference was lower than 2 °C, the assumption of isothermal conditions is reasonable. The temperature profiles are presented in Fig. S2.†

3 Kinetic model development and numerical simulation

3.1 Three-site surface reaction mechanism

The developed kinetic model is based on the DFT calculations of Studt *et al.*[30,31] for CO and CO_2 hydrogenation to methanol, and the WGSR. The adsorption energies of CO_2^* and H_2O^* were taken from Polierer *et al.*[32]

Studt *et al.*[30,31] applied the calculations on two stepped model surfaces: Cu (211), denoted in the presented mechanism as "site (a)", and a fully Zn-covered Cu (211), denoted "site (b)". The (211) facets were chosen, as it was found through experiments and theoretical calculations that they are the most active surfaces for the methanol synthesis.[18,22,24,30,31] Since surface defects scale linearly with the overall observed activity, the reactivity of other facets (*e.g.* 111) can be neglected.[24] Besides, from a modeling point of view, the consideration of a most representative (*i.e.* most active) single facet is desirable, because an additional considered facet would double the amount of reactions and surface species, which makes the model more complex and requires a higher computational effort.

In this work, all reaction paths studied by Studt *et al.*[30,31] were originally implemented and tested for different operating conditions. The initial tests confirmed remarks proposed by Studt *et al.*,[30] that CO hydrogenation on Cu/Zn (211) and CO_2 hydrogenation on Cu (211) are negligible. Therefore, CO hydrogenation on Cu/Zn (211) was eliminated from the final microkinetic model. The CO_2 hydrogenation on Cu (211), however, was kept in the model, as it describes the accumulation of formate on the Cu (211) surface, which reduces the number of free sites and could therefore slow down other reactions, *e.g.* CO hydrogenation.

Studt *et al.*[31] made DFT calculations for four WGS reaction pathways on both Cu (211) and Cu/Zn (211) surfaces: the redox mechanism, the water-assisted redox mechanism, the carboxyl mechanism, and the water-assisted carboxyl mechanism (totalizing eight possible reaction routes). After implementing and testing all these eight possible reaction pathways for different conditions, it was confirmed that the water-assisted carboxyl mechanism is dominant, and it is active on both Cu (211) and Cu/Zn (211). Thus, only this WGS reaction pathway (on both surfaces) is taken into account in the final kinetic model. After all, non-relevant reaction paths will only add complexity and increase the computational time of the simulations without contributing to the accuracy of the results.

It is known that formate (HCOO*) is able to cover a significant part of the catalyst surface, being an intermediate for CO_2 hydrogenation and inhibiting other reactions, such as CO hydrogenation.[30] It is, however, unlikely that formate inhibits hydrogen adsorption, because there should be still enough small sites available

between adsorbed formate. A comparable situation is seen in the ammonia synthesis, in which it was shown that the interaction (or inhibition) of nitrogen with hydrogen is not significant.[33,34] Another important feature is that, in the CO_2 hydrogenation, the decomposition of H_2COOH* into H_2CO* and $OH*$ would need an additional free site, and could therefore be inhibited by high formate concentrations. On the other hand, this does not seem to be realistic, as H_2COOH* is a large molecule that should not need extra space for its decomposition.[30] Therefore, a third Cu (211) site is considered in our model, denoted as "site (c)", which is available for hydrogen and water adsorption. Similar approaches were published by other groups.[15,16,30]

The final kinetic model takes into account 23 surface species, of which ten are related to Cu (211) [$CO_{(a)}$, $HCO_{(a)}$, $HCOO_{(a)}$, $HCOOH_{(a)}$, $H_2COOH_{(a)}$, $H_2CO_{(a)}$, $H_3CO_{(a)}$, $COOH_{(a)}$, $CO_{2(a)}$, site (a)], nine are related to Cu/Zn (211) [$CO_{(b)}$, $HCOO_{(b)}$, $HCOOH_{(b)}$, $H_2COOH_{(b)}$, $H_2CO_{(b)}$, $H_3CO_{(b)}$, $COOH_{(b)}$, $CO_{2(b)}$, site (b)] and four are related to site (c) [$H_{(c)}$, $OH_{(c)}$, $H_2O_{(c)}$, site (c)].

The reaction network of the carbon-containing species is shown in Fig. 2. It consists of five reaction pathways: CO hydrogenation on Cu (211), CO_2 hydrogenation on Cu (211), WGSR (water-assisted carboxyl mechanism) on Cu (211), CO_2 hydrogenation on Cu/Zn (211), and WGSR (water-assisted carboxyl mechanism) on Cu/Zn (211).

3.2 Kinetic equations

The catalyst surface is modeled considering a random distribution of the adsorbed species (mean-field approximation). A surface reaction is expressed as:

$$\sum_{i=1}^{N_g+N_s} \left(v'_{ik} \cdot \chi_i \right) \rightarrow \sum_{i=1}^{N_g+N_s} \left(v''_{ik} \cdot \chi_i \right) \tag{4}$$

$$\text{With } v_{ik} = v''_{ik} - v'_{ik} \tag{5}$$

Here, N_g and N_s are the number of gaseous and surface species, respectively, χ_i is the respective species i, v'_{ik} and v''_{ik} are the stoichiometric coefficients of the reactants and the
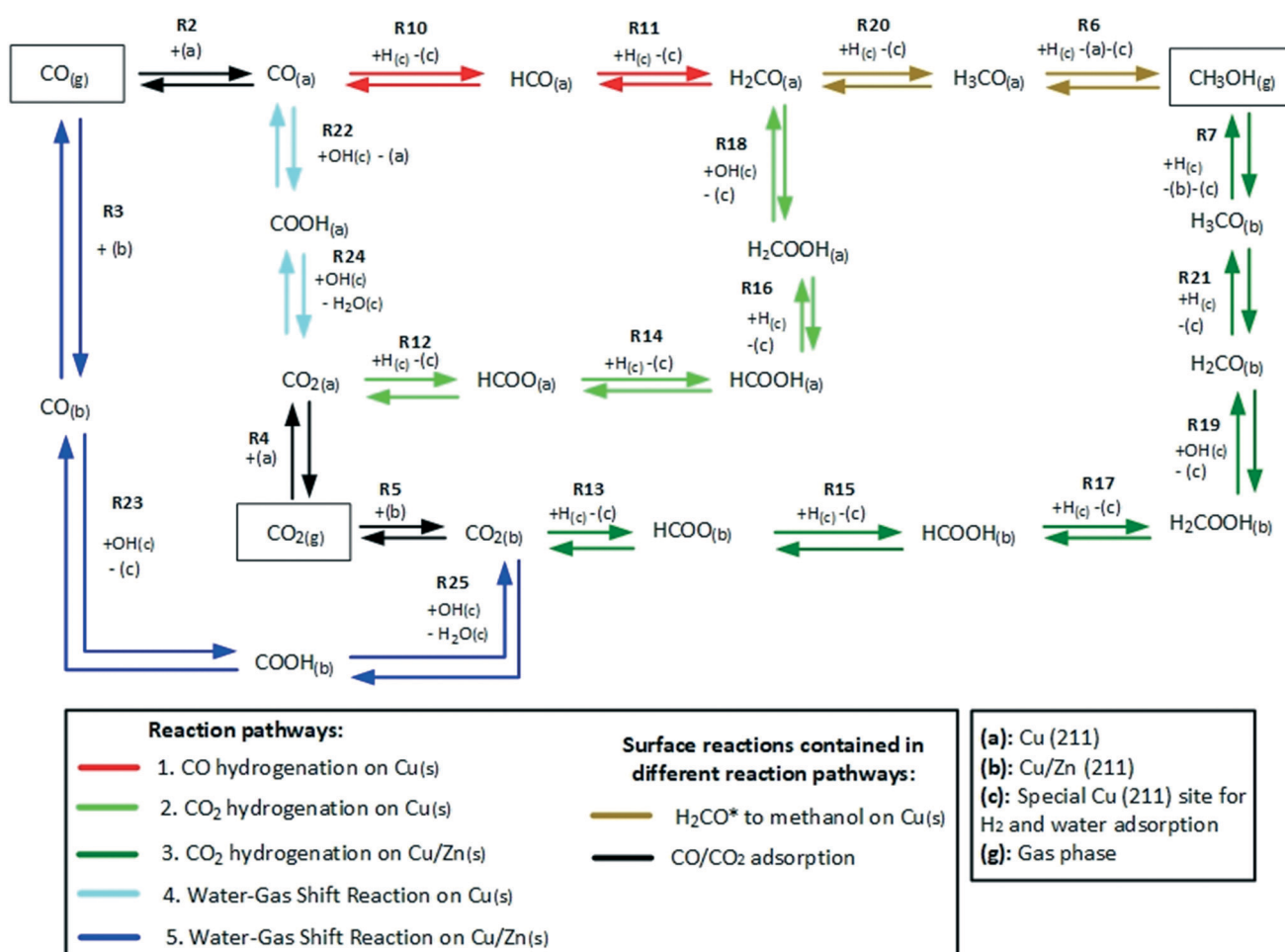

Fig. 2 Reaction network of the carbon-containing species in the methanol synthesis and the WGSR.

This journal is © The Royal Society of Chemistry 2021

React. Chem. Eng., 2021, **6**, 868–887 | 871

products (species i in reaction k), respectively, and ν_{ik} is the stoichiometric gain of species i in reaction k.

As the methanol synthesis is typically operated at elevated pressures (50–100 bar),[9] the ideal gas consideration may give partial pressures that differ significantly from the actual fugacities of the gases. Slotboom et al.[16] reported deviations up to 10% comparing ideal and real gas approaches. Therefore, the Peng–Robinson equation of state[35] is used in our model to calculate the fugacities, using binary interaction parameters (k_{ij}) and other necessary data reported in literature,[36,37] and including an effective hydrogen acentric factor ($\omega = -0.05$).[38]

In the present kinetic model, all surface species are considered to occupy a single site ($\sigma_i = 1$ for all species). The surface coverage of a species i (θ_i) on a specific active site represents the fraction of this site that is occupied by that species. The calculation of the surface coverages is shown in eqn (6), and the sum of all coverages from a specific site must be 1 (eqn (7)).

$$\theta_i = \frac{c_i \cdot \sigma_i}{\Gamma} \tag{6}$$

$$\sum \theta_{i(a)} = \sum \theta_{i(b)} = \sum \theta_{i(c)} = 1 \tag{7}$$

where c_i is the concentration of surface species i, σ_i is the number of surface sites occupied by species i, and Γ is the surface site density. The turnover rate r (eqn (8)) consists in three multiplying functions: one dependent on temperature (F_T),[39,40] one dependent on the gaseous species fugacities (F_G), and one dependent on the surface species coverages (F_S).

$$r = F_T \cdot F_G \cdot F_S \tag{8}$$

$$F_T = T^{(1+\beta)} \cdot \frac{k_b}{h} \cdot \exp\left(-\frac{E_A}{R \cdot T} + \frac{\Delta S^{\neq}}{R}\right) \tag{9}$$

$$F_G = \prod_{j=1}^{N_g} \left[\left(\frac{f_j}{p_0}\right)^{\nu_j}\right] \tag{10}$$

$$F_S = \prod_{i=N_g+1}^{N_g+N_s} \left[(\phi_i \cdot \theta_i)^{\nu_i}\right] \tag{11}$$

Here, T is the reaction temperature, β is a correction due to the thermodynamic consistency (see section 3.3), k_b is the Boltzmann constant, h is the Planck constant, E_A is the reaction activation energy, $\Delta S^{\neq}$ is the reaction entropy barrier, f_j is the fugacity of the gas component j, p_0 is the reference pressure (1 bar), R is the universal gas constant, and θ_i is the surface coverage of species i. ϕ_i represents the fraction of the site type of surface species i in relation to the total number of sites for carbon-containing compounds (sites a and b). Substituting eqn (9)–(11) into eqn (12), the turnover rate of a reversible reaction k is:

$$r_k = T^{(1+\beta_k^+)} \cdot \frac{k_b}{h} \cdot \exp\left(-\frac{E_{A,k}^+}{R \cdot T} + \frac{\Delta S_k^{\neq,+}}{R}\right) \tag{12}$$
$$\cdot \prod_{j=1}^{N_g} \left[\left(\frac{f_j}{p_0}\right)^{\nu'_{j,k}}\right] \cdot \prod_{i=N_g+1}^{N_g+N_s} \left[(\phi_i \cdot \theta_i)^{\nu'_{i,k}}\right]$$
$$- T^{(1+\beta_k^-)} \cdot \frac{k_b}{h} \cdot \exp\left(-\frac{E_{A,k}^-}{R \cdot T} + \frac{\Delta S_k^{\neq,-}}{R}\right)$$
$$\cdot \prod_{j=1}^{N_g} \left[\left(\frac{f_j}{p_0}\right)^{\nu''_{j,k}}\right] \cdot \prod_{i=N_g+1}^{N_g+N_s} \left[(\phi_i \cdot \theta_i)^{\nu''_{i,k}}\right]$$

where the superscripts + and − refer to the forward and the reverse reaction, respectively. The reaction rate is related to the turnover rate by:

$$\dot{s}_k = r_k \cdot \Gamma \tag{13}$$

The dependency of (ϕ_i) to the site type is shown in Table 1. The estimation of the zinc coverage (ϕ_{Zn}) is discussed in section 3.3.

3.3 Thermodynamic consistency

The microkinetic model has to correctly predict the thermodynamic equilibrium. The objective of the thermodynamic consistency corrections is to ensure reversibility of each elementary step according to the properties of the gas-phase species involved, which are known. The method described here is an adapted version of an approach developed in the Deutschmann's group,[41,42] considering a temperature operating range between $T_1 = 200$ °C and $T_2 = 300$ °C.

Goos et al.[43] reported thermodynamic data of gas species involved in the methanol synthesis. The free Gibbs energy function G_j^0 of each gas species j at the reference pressure of 1 bar is:

$$G_j^0(T)$$
$$= R \cdot \left[a_{6,j} + (a_{1,j} - a_{7,j}) \cdot T - \frac{a_{2,j}}{2} \cdot T^2 - \frac{a_{3,j}}{6} \cdot T^3 - \frac{a_{4,j}}{12} \cdot T^4 - \frac{a_{5,j}}{20} \cdot T^5 - a_{1,j} \cdot T \cdot \ln(T)\right] \tag{14}$$

Here, $a_{1-7,j}$ are compound-specific constants.[43] The free Gibbs energy variation of the three global reactions (eqn (15)–(17)) is:

$$\Delta G_{COHyd.}^0(T) = G_{CH_3OH}^0(T) - G_{CO}^0(T) - 2 \cdot G_{H_2}^0(T) \tag{15}$$

Table 1   Values of ϕ_i depending on the site type

Site type	ϕ_i
Site (a)	$(1 - \phi_{Zn})$
Site (b)	ϕ_{Zn}
Site (c)	1

$$\Delta G^0_{\text{CO}_2\text{Hyd.}}(T) = G^0_{\text{CH}_3\text{OH}}(T) + G^0_{\text{H}_2\text{O}}(T) - G^0_{\text{CO}_2}(T) - 3\cdot G^0_{\text{H}_2}(T) \quad (16)$$

$$\Delta G^0_{\text{WGSR}}(T) = G^0_{\text{CO}_2}(T) + G^0_{\text{H}_2}(T) - G^0_{\text{CO}}(T) - G^0_{\text{H}_2\text{O}}(T) \quad (17)$$

The assumption of constant heat capacity (c_p) was made for the global reactions in the temperature range of 200 to 300 °C. With this consideration, the Gibbs function was reduced from seven to three parameters (A_{1-3}) (eqn (18) and (19)) with the least square regression method (eqn (20)).

$$\Delta G^0_{m,3p}(T) = (\Delta H^0_{\text{Tr},m} - \Delta c_{p,m}\cdot T_r) + (\Delta c_{p,m} + \Delta c_{p,m}\cdot \ln T_r - \Delta S^0_{\text{Tr},m})$$
$$\cdot T + (-\Delta c_{p,m})\cdot T\cdot \ln T \quad (18)$$

$$\Delta G^0_{m,3p}(T) = A_{1,m} + A_{2,m}\cdot T + A_{3,m}\cdot T\cdot \ln T \quad (19)$$

$$\min\left[\int_{T_1}^{T_2}\left(\Delta G^0_{m,7p}(T) - \Delta G^0_{m,3p}(T)\right)^2 dT\right] \quad (20)$$

where $\Delta G^0_{m,3p}$ is the Gibbs energy change of the global reaction m considering three parameters, $\Delta H^0_{\text{Tr},m}$ and $\Delta S^0_{\text{Tr},m}$ are the enthalpy and entropy change of the global reaction m at the standard temperature ($T_r = 298.15$ K), $\Delta c_{p,m}$ is the heat capacity change of the global reaction m, and $A_{1-3,m}$ are the regression parameters 1–3 of the global reaction m.

The estimated regression parameters are summarized in Table S2.† When comparing the three-parameter functions with the seven-parameter ones, the average relative error of $\Delta G^0_{m,3p}$ was below 0.002%, and the maximum relative error was 0.007%. Therefore, a constant heat capacity sufficiently describes the free Gibbs energy change of the reactions involved in the methanol synthesis between 200 and 300 °C.

From DFT calculations, the free Gibbs energy change ($\Delta G^0_{k,\text{DFT}}$) of a reversible surface reaction k is given in the form:

$$\Delta G^0_{k,\text{DFT}}(T) = (E^+_{A,k} - E^-_{A,k}) - T\cdot(\Delta S^{\neq,+}_k - \Delta S^{\neq,-}_k) \quad (21)$$

The free Gibbs energy change ($\Delta G^0_{k,\text{DFT}}$) of a global reaction pathway m (described in Fig. 2) is then calculated:

$$\Delta G^0_{m,\text{DFT}}(T) = \sum_{k=1}^{N_r} \zeta_{k,m}\cdot \Delta G^0_k(T)$$
$$= \sum_{k=1}^{N_r} \zeta_{k,m}\cdot\left[\left(E^+_{A,k} - E^-_{A,k}\right) - T\cdot\left(\Delta S^{\neq,+}_k - \Delta S^{\neq,-}_k\right)\right] \quad (22)$$

Here, N_r is the number of reactions, $\zeta_{k,m}$ is the stoichiometric coefficient of a reversible surface reaction k in the global reaction pathway m.

In eqn (21) and (22) there is no term multiplying $T\cdot\ln(T)$ for $\Delta G^0_{m,\text{DFT}}$, like there is in eqn (18) and (19) for $\Delta G^0_{m,3p}$. Each $\Delta G^0_{m,\text{DFT}}$ needs to be modified with the

addition of parameter β multiplying $T\cdot\ln(T)$, so that the equations are able to match. The calculation of β can also be seen in other thermodynamic consistency processes of surface kinetic mechanisms reported in literature.[41,42] The new free Gibbs energy change ($\Delta G^{0,\text{TC}}_{m,\text{DFT}}$) is calculated with the corrected terms ($E^{+,\text{TC}}_{A,k}$, $E^{-,\text{TC}}_{A,k}$, $\Delta S^{\neq,+,\text{TC}}_k$, $\Delta S^{\neq,-,\text{TC}}_k$, $\beta^{+,\text{TC}}_k$, $\beta^{-,\text{TC}}_k$), as shown in eqn (23), and these terms are estimated so that eqn (24) holds for all reaction pathways:

$$\Delta G^{0,\text{TC}}_{m,\text{DFT}}(T)$$
$$= \sum_{k=1}^{N_r} \zeta_{k,m}\cdot\left[\left(E^{+,\text{TC}}_{A,k} - E^{-,\text{TC}}_{A,k}\right) - T\cdot\left(\Delta S^{\neq,+,\text{TC}}_k - \Delta S^{\neq,-,\text{TC}}_k\right) - T\cdot\ln(T)\cdot\left(\beta^{+,\text{TC}}_k - \beta^{-,\text{TC}}_k\right)\right]$$
$$(23)$$

$$\Delta G^{0,\text{TC}}_{m,\text{DFT}}(T) = \Delta G^0_{m,3p}(T) \quad (24)$$

In eqn (24), the two functions will only be equal for a range of different temperatures (200–300 °C) if their corresponding terms match, namely the independent terms (eqn (25)), the terms accompanying T (eqn (26)), and terms accompanying $T\cdot\ln(T)$ (eqn (27)).

$$q_{1,m} = A_{1,m} - \sum_{k=1}^{N_r} \zeta_{k,m}\cdot\left(E^{+,\text{TC}}_{A,k} - E^{-,\text{TC}}_{A,k}\right) = 0 \quad (25)$$

$$q_{2,m} = A_{2,m} - \sum_{k=1}^{N_r} \zeta_{k,m}\cdot\left(\Delta S^{\neq,+,\text{TC}}_k - \Delta S^{\neq,-,\text{TC}}_k\right) = 0 \quad (26)$$

$$q_{3,m} = A_{3,m} - \sum_{k=1}^{N_r} \zeta_{k,m}\cdot\left(\beta^{+,\text{TC}}_k - \beta^{-,\text{TC}}_k\right) = 0 \quad (27)$$

where $q_{1-3,m}$ represent the thermodynamic constraints. As in most microkinetic models, this is an underdetermined algebraic system, because there are 150 variables (6 parameters × 25 reactions) and only 15 equations (eqn (25)–(27)) for the five reaction pathways. Herrera Delgado et al.[42] proposed an objective function that minimizes the individual corrections of E_A, the pre-exponential factor (a term which contains $\Delta S^{\neq}$), and β. In this work, however, it was preferred to minimize the difference between the corrected Gibbs energy barrier ($\Delta G^{\neq,\text{TC}} = E^{\text{TC}}_A - T\Delta S^{\neq\text{TC}} - T\cdot\ln T\cdot\beta^{\text{TC}}$) and the original DFT-based one ($G^{\neq,\text{Orig}} = E^{\text{Orig}}_A - T\cdot\Delta S^{\neq,\text{Orig}}$), for both forward and reverse reactions. This approach was chosen, because the model is more sensitive to modifications in the $\Delta G^{\neq}$ than in its individual parameters. Besides, the model is also sensitive to ΔG changes of all surface reactions ($\Delta G = \Delta G^{\neq,+} - \Delta G^{\neq,-}$), even fast steps usually in equilibrium, as changing the ΔG will alter this equilibrium, which affects the whole mechanism. The constrained objective function is shown in eqn (28).

This journal is © The Royal Society of Chemistry 2021

React. Chem. Eng., 2021, 6, 868–887 | 873

$$f_{\text{obj}} = \min \int_{T_1}^{T_2} \left\{ \sum_{k=1}^{N_r} w_k \cdot \left\{ \left[E_{A,k}^{+,\text{TC}} - T \cdot \left(\Delta S_k^{\neq,+,\text{TC}} + \ln(T) \cdot \beta_k^{+,\text{TC}} \right) - \left(E_{A,k}^{+,\text{Orig.}} - T \cdot \Delta S_{fk}^{\neq,\text{Orig.}} \right) \right]^2 + \left[E_{A,k}^{-,\text{TC}} - T \cdot \left(\Delta S_k^{\neq,-,\text{TC}} + \ln(T) \cdot \beta_k^{-,\text{TC}} \right) - \left(E_{A,k}^{-,\text{Orig.}} - T \cdot \Delta S_k^{\neq,-,\text{Orig.}} \right) \right]^2 \right\} \right\} dT \quad (28)$$

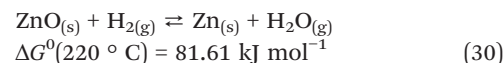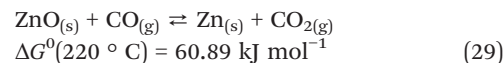$$\text{Subject to}: \quad q_{1,m} = q_{2,m} = q_{3,m} = 0 \quad m = 1:5$$

Here, w_k are selectable weights, which are chosen to protect the most sensitive reactions against changes. In this work, the weights of reactions R1, R2, R14, R16, and R17 were set to 10^5 and the other weights were set to one. This minimization problem can be solved with the method of the Lagrange multipliers (further explanation is given in the ESI†).

In Fig. 3, the capability of the model to predict the equilibrium is presented. The methanol concentration of the equilibrium for different operating conditions is calculated with Aspen Plus, using the RGibbs approach. Simulations with the same operating conditions are made with the microkinetic model considering a sufficiently long PFR, in order to achieve the equilibrium. When comparing the values, the conclusion is that the equilibrium is accurately predicted by the model, and the slight overestimations are probably due to rounding numbers and small differences in the thermodynamic data.

3.4 Estimation of the active sites distribution

A significant number of experimental observations have shown that the different active sites of the Cu/ZnO-based catalysts are adjusted dynamically to the operating conditions.[27,44] It is therefore relevant to correctly model this phenomenon, in order to estimate the fraction of Cu (site a) and Cu/Zn (site b) on the surface for different operating conditions. After all, this quantification has a high impact on the simulation of the methanol synthesis.

The formation of a Cu–Zn alloy by reduction of zinc oxide and migration to the copper bulk can be described by the following reactions:[13,29]

Fig. 3 Methanol equilibrium concentration calculated with Aspen Plus and with the microkinetic model. Operating conditions: 60 bar, and a feed concentration of H_2/CO_x = 80/20% v/v.

$$ZnO_{(s)} + CO_{(g)} \rightleftharpoons Zn_{(s)} + CO_{2(g)}$$
$$\Delta G^0(220\ ^\circ C) = 60.89\ \text{kJ mol}^{-1} \quad (29)$$

$$ZnO_{(s)} + H_{2(g)} \rightleftharpoons Zn_{(s)} + H_2O_{(g)}$$
$$\Delta G^0(220\ ^\circ C) = 81.61\ \text{kJ mol}^{-1} \quad (30)$$

Kuld *et al.*[29] proposed a detailed method to estimate the zinc fraction on the surface of the catalyst. First, the solubility of zinc in the Cu-bulk (X_{Zn}) is calculated considering the equilibrium of the zinc reduction *via* carbon monoxide (eqn (29)). The effect of the lower atom coordination in nanoparticles was considered for both, zinc oxide and copper.

$$\ln(X_{Zn}) = -\frac{\Delta G_{Zn\ red.}^0(T)}{R \cdot T} - \ln(\gamma_{Zn}) + \ln\left(\frac{a_{CO}}{a_{CO_2}}\right)$$
$$+ 4 \cdot \frac{\bar{\gamma}_{ZnO} \cdot M_{ZnO}}{d_{ZnO} \cdot \rho_{ZnO} \cdot R \cdot T} - 4 \cdot \frac{\bar{\gamma}_{Cu} \cdot M_{Cu}}{d_{Cu} \cdot \rho_{Cu} \cdot R \cdot T} + \ln(a_{ZnO}) \quad (31)$$

where $\Delta G_{Znred.}^0(T)$ is the free Gibbs energy change in the zinc reduction *via* CO at the reference pressure (1 bar) and the reaction temperature T, γ_{Zn} is the activity coefficient of zinc in Cu, a_{CO_2} and a_{CO} are the activities of CO_2 and CO respectively, $\bar{\gamma}_{ZnO}$ and $\bar{\gamma}_{Cu}$ represent the respective surface energy of zinc oxide and copper, M_{ZnO} and M_{Cu} are the molar masses of zinc oxide and copper, d_{ZnO} and d_{Cu} are the crystallite diameter of zinc oxide and copper, ρ_{ZnO} and ρ_{Cu} are the density of zinc oxide and copper, and a_{ZnO} is the activity of zinc oxide. The values of activity coefficient, surface energies and crystallite diameters were reported by Kuld *et al.*[29]

The activity of the zinc oxide is assumed to be 1. Although not specifically noted by the authors, this assumption has probably been made considering that the typical quantity of metallic zinc in the copper bulk is not significant compared to the zinc oxide bulk.

In typical industrial methanol production, the WGSR is generally in equilibrium. Therefore, as the free Gibbs energy change of the reduction of zinc *via* hydrogen (eqn (30)) is significantly higher than *via* carbon monoxide (eqn (29)), the most probable way that hydrogen and water affect the reduction of zinc is by changing the a_{CO}/a_{CO_2} ratio through the WGSR. Kuld *et al.*[29] proposed an effective a_{CO}/a_{CO_2} ratio to be used in eqn (31) to account for the H_2/H_2O effect.

$$\left(\frac{a_{CO}}{a_{CO_2}}\right)_{\text{eff}} = \frac{a_{CO} \cdot a_{H_2}}{a_{CO_2} \cdot a_{H_2O}} \cdot \frac{1}{K_{WGSR}(T)} \quad (32)$$

Here, K_{WGSR} is the equilibrium constant of the WGSR. The segregation of metallic zinc from the Cu-bulk into the catalyst surface is then considered (eqn (33)).
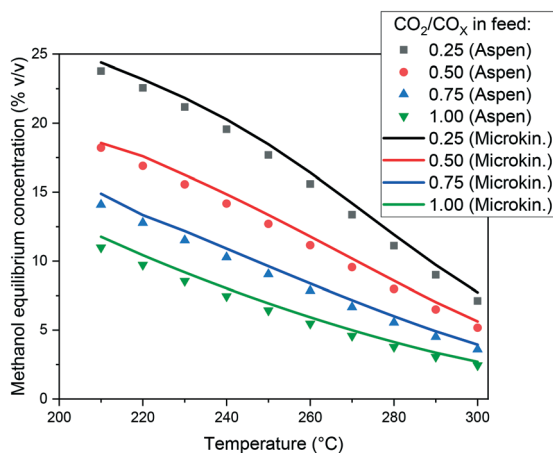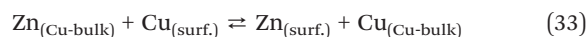
$$Zn_{(Cu\text{-}bulk)} + Cu_{(surf.)} \rightleftharpoons Zn_{(surf.)} + Cu_{(Cu\text{-}bulk)} \quad (33)$$

874 | *React. Chem. Eng.*, 2021, **6**, 868–887

This journal is © The Royal Society of Chemistry 2021

Kuld *et al.*[29] performed DFT calculations of this segregation on different facets, taking into account Zn–Zn interactions. For the facet Cu (211), the authors reported enthalpy variations (ΔH^0_{seg}) of −27.01 kJ mol^{-1} for a Zn-free surface, −18.36 kJ mol^{-1} for a 0.333 Zn monolayer (ML), and −8.71 kJ mol^{-1} for a 0.667 Zn monolayer (ML). The ΔH^0_{seg} is then calculated (in kJ mol^{-1}) as a function of the zinc coverage on the surface (ϕ_{Zn}):

$$\Delta H^0_{seg} = -27.01 \cdot (1 - \phi_{Zn}) \tag{34}$$

The entropy change (ΔS^0_{seg}) of the segregation process on a Cu (211) facet was estimated to be 7.1 J mol^{-1} K^{-1}, and effects of Zn–Zn interactions in the entropy were neglected.[29] The zinc coverage on the surface (ϕ_{Zn}) is calculated by solving eqn (35), in which it is considered that the segregation of zinc to the surface is in equilibrium.

$$K_{seg} = \frac{\phi_{Zn} \cdot (1 - X_{Zn})}{X_{Zn} \cdot (1 - \phi_{Zn})} = \exp\left[\frac{-\left(\Delta H^0_{seg} - T \cdot \Delta S^0_{seg}\right)}{R \cdot T} \right] \tag{35}$$

The activities of the gases can be represented by their fugacities. The ratio $a_{CO} \cdot a_{H_2} / (a_{CO_2} \cdot a_{H_2O})$, or better $f_{CO} \cdot f_{H_2} / (f_{CO_2} \cdot f_{H_2O})$, represent the gas reducing power (GRP). Kuld *et al.*[29] showed that the described method agrees well with experimental data in a GRP range between 0 to 15, which roughly corresponds to a ϕ_{Zn} range between 0 and 0.30 (for a Cu (211) facet), and a X_{Zn} range between 0 and 0.003. However, the actual GRP of typical methanol synthesis operations may be higher than 15, especially at a CO-rich syngas condition, in which the amount of water is significantly low. For example, for a synthesis gas containing H$_2$/CO/CO$_2$/CH$_3$OH/H$_2$O/N$_2$ = 60/22/5/1/0.3/11.9% v/v, the GPR would be 880. In this case, it is assumed that the zinc concentration in the copper bulk may be more significant, causing a non-negligible reduction of the zinc oxide bulk, and thus affecting its activity.

Thus, the value for the ZnO activity coefficient is limited by the segregation of zinc to the copper bulk, and a linear relation between a_{ZnO} and X_{Zn} is made (eqn (36)), in order to extend the application range of the method from Kuld *et al.*[29] for higher GRP.

$$a_{ZnO} = 1 - \alpha \cdot X_{Zn} \tag{36}$$

Here, α express this linear relation, and a value of $\alpha = 1.5$ is chosen, which roughly correspond to a maximum zinc coverage of 0.90, a limit value proposed elsewhere.[15] Substituting eqn (36) into eqn (31), representing the gas activities by their fugacities, and reorganizing the equation, the fraction of zinc in the copper bulk (X_{Zn}) is:

In Fig. 4, the original and the modified functions are compared for different GRP at the temperatures of 220 and 250 °C. In Fig. 4A and C, the solubility of zinc in the Cu-bulk is shown, while in Fig. 4B and D the zinc coverage is presented. It is show that the modified function attenuate X_{Zn} and ϕ_{Zn} at a high GRP, while not influencing X_{Zn} and ϕ_{Zn} significantly at low GRP.

Finally, at CO$_2$-rich operating conditions, the reverse water-gas shift reaction (rWGSR) is normally faster than the WGSR, and is usually not in equilibrium. In this case, the contribution of the direct reduction of ZnO by H$_2$ is probably higher, and a more complex analysis must be made.[29] In order to keep using the method proposed by Kuld *et al.*,[29] it was chosen to set a minimum zinc coverage of 0.30 to avoid underestimations of zinc coverage by these conditions.

3.5 Estimation of the active catalytic area

Because of the dynamic behavior of the Cu/ZnO/Al$_2$O$_3$ and the three-site approach, characterization tests (*e.g.* N$_2$O chemisorption) can just estimate an initial active catalytic area, since it changes depending on the experimental conditions. Still, these estimations serve as a reference in comparing different catalysts. The determination of the surface site density is a challenge for the same reason. Therefore, it was chosen to use the experimental data to estimate a specific catalyst site quantity ($n_{M,Cat}$) in terms of mol of active sites per catalyst mass unit (eqn (38)). The total active surface area (A_{Cat}) is then calculated by eqn (39).

$$n_{M,Cat} = \frac{\text{Number of active sites (mol)}}{\text{Catalyst mass (kg)}} \tag{38}$$

$$A_{Cat} = \frac{n_{M,Cat} \cdot m_{Cat}}{\Gamma} \tag{39}$$

Here, m_{Cat} is the mass of the catalyst inside the reactor. By estimating the $n_{M,Cat}$, the need to quantify the surface site density (Γ) is avoided, as shown in the next section.

The $n_{M,Cat}$ is estimated by minimizing the prediction errors of the methanol output with the experimental data. When the experimental data has values differ significantly (*e.g.* 0.08% v/v and 12.00% v/v), a better distribution of each point's importance can be made with introducing weights. Common approaches are the inverse of squared experimental value,[45,46] the inverse of the squared simulated value,[47] or the inverse of experimental multiplied by simulated value.[48] Here, the inverse of the squared experimental value was used as weights. The function fminsearch from Matlab was used, and the objective function is shown as follows.

$$X_{Zn} = \left\{ \frac{f_{CO_2} \cdot f_{H_2O}}{f_{CO} \cdot f_{H_2}} \cdot K_{WGSR}(T) \cdot \gamma_{Zn} \cdot \exp\left[\frac{1}{R \cdot T} \cdot \left(\Delta G^0_{Zn\,red.}(T) - 4 \cdot \frac{\overline{\gamma}_{ZnO} \cdot M_{ZnO}}{d_{ZnO} \cdot \rho_{ZnO}} + 4 \cdot \frac{\overline{\gamma}_{Cu} \cdot M_{Cu}}{d_{Cu} \cdot \rho_{Cu}} \right) \right] + \alpha \right\}^{-1} \tag{37}$$

This journal is © The Royal Society of Chemistry 2021

React. Chem. Eng., 2021, **6**, 868–887 | 875

$$f_{\text{obj}} = \sum_{n=1}^{N_\text{p}} \left(\frac{y^n_{\text{CH}_3\text{OH,out}} - \hat{y}^n_{\text{CH}_3\text{OH,out}}}{y^n_{\text{CH}_3\text{OH,out}}} \right)^2 \quad (40)$$

Here, $y^n_{\text{CH}_3\text{OH,out}}$ and $\hat{y}^n_{\text{CH}_3\text{OH,out}}$ are the experimental and simulated value of point n, respectively.

3.6 Reactor equations

In this work, the microkinetic model is applied to simulate steady-state operation of two types of reactor: a fixed-bed tube reactor (own experiments and literature data[14,16]) and a CSTR (literature data[15]). Isothermal operation was considered in both cases.

3.6.1 Fixed-bed tube reactor. In the tube reactor model, only variations along the reactor length are assumed, given the ratio between the diameter of the reactor and the particle size ($24 \leq d_\text{R}/d_\text{p} \leq 48$). The influence of back-mixing is neglected (plug flow reactor assumption, PFR). A total molar balance along the catalyst bed length (L) is calculated:

$$\frac{\text{d}\dot{n}}{\text{d}z} = \frac{1}{L} \cdot \sum_{j=1}^{N_\text{g}} \sum_{k=1}^{N_\text{r}} \left[A_{\text{Cat}} \cdot \left(v'_{jk} \cdot \dot{s}_{\text{f}k} - v''_{jk} \cdot \dot{s}_{\text{r}k} \right) \right] \quad (41)$$

where $\dot{n}$ is the total gas mole flow, z is the axial direction, N_r is the number of reactions. Substituting eqn (13) and (39) in eqn (41):

$$\frac{\text{d}\dot{n}}{\text{d}z} = \frac{1}{L} \cdot \sum_{j=1}^{N_\text{g}} \sum_{k=1}^{N_\text{r}} \left[\frac{n_{\text{M,Cat}} \cdot m_{\text{Cat}}}{\Gamma} \cdot \left(v'_{jk} \cdot r_{\text{f}k} \cdot \Gamma - v''_{jk} \cdot r_{\text{r}k} \cdot \Gamma \right) \right] \quad (42)$$

$$\frac{\text{d}\dot{n}}{\text{d}z} = \frac{1}{L} \cdot \sum_{j=1}^{N_\text{g}} \sum_{k=1}^{N_\text{r}} \left[n_{\text{M,Cat}} \cdot m_{\text{Cat}} \cdot \left(v'_{jk} \cdot r_{\text{f}k} - v''_{jk} \cdot r_{\text{r}k} \right) \right] \quad (43)$$

The axial reactor profile of the molar fraction of each gaseous species j (y_j) is calculated *via* a component balance of the gas phase.

$$\frac{\text{d}y_j}{\text{d}z} = \frac{1}{\dot{n}} \cdot \left\{ \frac{1}{L} \cdot \sum_{k=1}^{N_\text{r}} \left[n_{\text{M,Cat}} \cdot m_{\text{Cat}} \cdot \left(v'_{jk} \cdot r_{\text{f}k} - v''_{jk} \cdot r_{\text{r}k} \right) \right] - y_j \cdot \frac{\text{d}\dot{n}}{\text{d}z} \right\} \quad (44)$$

The coverage θ_i of each surface species i at a certain point in time is calculated *via* a component balance of the surface.

$$\frac{\text{d}\theta_i}{\text{d}t} = \sum_{k=1}^{N_\text{r}} \left(v'_{ik} \cdot r_{\text{f}k} - v''_{ik} \cdot r_{\text{r}k} \right) \quad (45)$$

Comments on solving this system of differential equations are given in the ESI.†

3.6.2 Continuous stirred tank reactor. In the CSTR model, a total molar balance in the reactor is calculated:

$$\frac{\text{d}n}{\text{d}t} = \dot{n}_{\text{in}} - \dot{n}_{\text{out}} + \sum_{j=1}^{N_\text{g}} \sum_{k=1}^{N_\text{r}} \left[n_{\text{M,Cat}} \cdot m_{\text{Cat}} \cdot \left(v'_{jk} \cdot r_{\text{f}k} - v''_{jk} \cdot r_{\text{r}k} \right) \right] \quad (46)$$
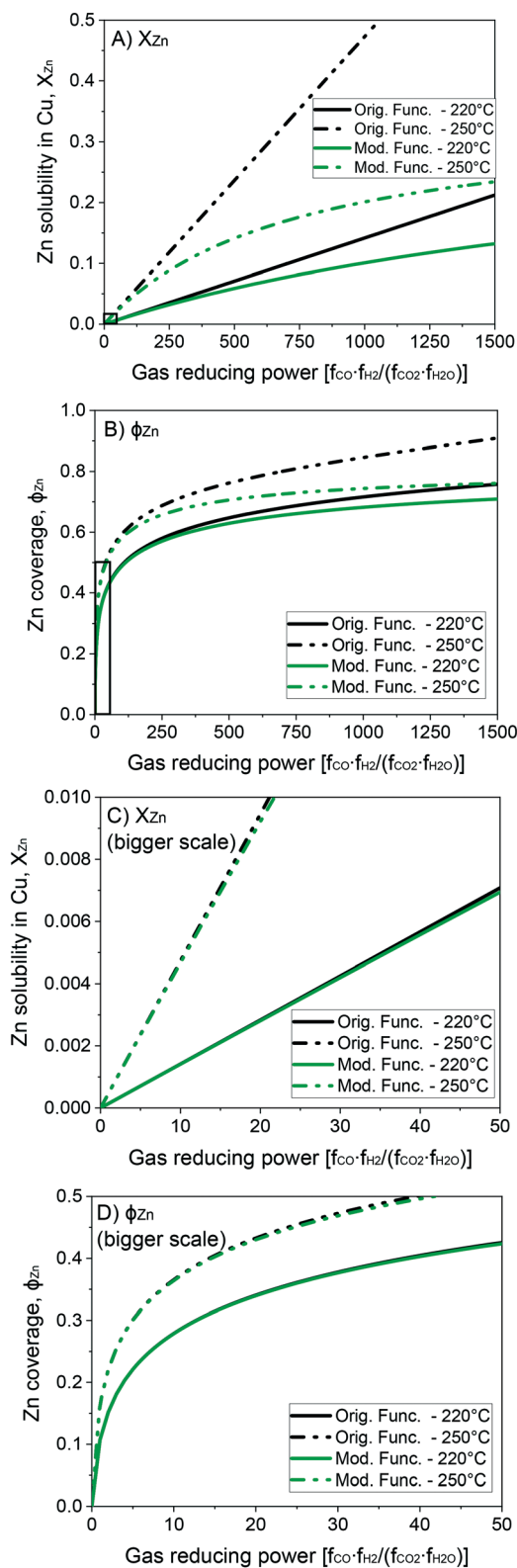

Fig. 4 Solubility of zinc in the Cu-bulk (A and C) and zinc coverage (B and D) as functions of the gas reducing power.

where dn/dt is the total mole accumulation in time, $\dot{n}_{in}$ is the mole flow entering the reactor, and $\dot{n}_{out}$ is the mole flow leaving the reactor. Assuming no gas accumulation in the reactor:

$$\dot{n}_{out} = \dot{n}_{in} + \sum_{j=1}^{N_g} \sum_{k=1}^{N_r} \left[n_{M,Cat} \cdot m_{Cat} \cdot \left(v'_{jk} \cdot r_{fk} - v''_{jk} \cdot r_{rk} \right) \right] \quad (47)$$

The component mole balance in the reactor is calculated:

$$\frac{dy_j}{dt} = \frac{1}{n} \cdot \left\{ \dot{n}_{in} \cdot y_{j,in} - \dot{n}_{out} \cdot y_j + \sum_{k=1}^{N_r} \left[n_{M,Cat} \cdot m_{Cat} \cdot \left(v'_{jk} \cdot r_{fk} - v''_{jk} \cdot r_{rk} \right) \right] \right\} \quad (48)$$

where dy_j/dt is the change in time of the mole fraction of component j, n is the total mole quantity in the gas phase, $y_{j,in}$ is the mole fraction of component j entering the reactor, and y_j is the mole fraction of component j in the reactor. The mole quantity in the gas phase can be calculated with the Peng–Robinson equation of state.[35]

Like in the PFR, the coverages of the surface species are calculated by:

$$\frac{d\theta_i}{dt} = \sum_{k=1}^{N_r} \left(v'_{ik} \cdot r_{fk} - v_{ik} \cdot r_{rk} \right) \quad (49)$$

Comments on solving this system of differential equations are given in the ESI.†

3.7 Sensitivity analysis

In order to evaluate the most sensitive reaction rate parameters in the kinetic model, the Campbell degree of rate control (DRC) method was applied.[49,50] This method consists in slightly changing the Gibbs energy (G_i) of a surface intermediate or a transition state, while keeping the Gibbs energy of the other species $G_{w \neq i}$ constant, and it has the advantage of maintaining the thermodynamic consistency of the model. For a set of reversible reactions, the degree of rate control of surface species or a transition state i (DRC_i) is defined as:

$$DRC_i = \left[\frac{\partial \ln \left(r_{CH_3OH,prod.} \right)}{\partial \ln (k_i)} \right]_{G^0_{w \neq i}}$$
$$= \left[-\frac{R \cdot T}{r_5 + r_6} \cdot \frac{\partial (r_5 + r_6)}{\partial \left(G^0_i \right)} \right]_{G^0_{w \neq i}} \quad (50)$$

Here, $(r_5 + r_6)$ is the methanol production rate, and G^0_i is the free Gibbs energy of species i at the reference pressure (1 bar). The method of finite differences is used as an approximation to solve eqn (50), and a step $\delta = 0.01$ kJ mol^{-1} was chosen. Eqn (51) is used to calculate the sensitivity of methanol generation, and eqn (52) is used for sensitivity of CO generation, which makes sense at high CO_2 content.

$$DRC_i \approx \frac{-R \cdot T}{\delta \cdot (r_6 + r_7)} \cdot \left\{ \left[r_6 \left(G^0_i + \delta \right) + r_7 \left(G^0_i + \delta \right) \right] - \left[r_6 \left(G^0_i \right) + r_7 \left(G^0_i \right) \right] \right\} \quad (51)$$

$$DRC_i \approx \frac{-R \cdot T}{\delta \cdot (-r_2 - r_3)} \cdot \left\{ \left[-r_2 \left(G^0_i + \delta \right) - r_3 \left(G^0_i + \delta \right) \right] - \left[-r_2 \left(G^0_i \right) - r_3 \left(G^0_i \right) \right] \right\} \quad (52)$$

4 Results and discussion

4.1 Model validation

A microkinetic model for syngas ($H_2/CO/CO_2$) conversion to methanol including a three-site approach and structural changes was successfully developed. The complete set of 25 reversible reactions and their respective parameters to calculate the turnover rates are summarized in Table 2. The thermodynamic consistency of the model was ensured (see section 3.3). The estimated value of the catalytic site quantity ($n_{M,cat}$) is 2.00 mol kg$_{cat.}^{-1}$.

The validation of the model was done using own experiments and data from literature.[14–16] The operating conditions in the respective setups are significantly different from ours, which contributes to a broader validation range. In Table 3, the operating conditions of each setup is summarized. For the data from Seidel et al.[15] with H_2/CO in feed, our model was initially overestimating methanol formation. Feeds with only H_2/CO are an extreme case, when looking at the zinc coverage. As the catalyst used is not exactly the same, we assume that in the experiments of Seidel et al.[15] zinc is covering more surface, leaving less Cu sites for the CO hydrogenation. By adjusting the value of α to 1.17 (see eqn (36)) in this specific case, roughly corresponding to a maximum of 95% zinc coverage, the measurements from Seidel et al.[15] with H_2/CO were reasonably predicted.

In Fig. 5, the normalized residues of the original model are shown for each carbon-containing species. By comparing simulations with experimental data, it was found that the WGSR is adequately predicted. However, if the operating conditions favor rWGSR, generally for feed ratios of CO_2/CO_X ($\bar{y}_{CO_2,0}$) higher than 0.65 ($CO_X = CO + CO_2$), the simulation of CO production through the rWGSR was significantly higher than the experimental values, as shown in Fig. 5A. This suggests that the Gibbs energy barrier ($\Delta G^{\neq} = E_A - T \cdot \Delta S^{\neq}$) is influenced by higher concentrations of CO_2 and H_2O or by surface intermediates derived from them, namely HCOO* and OH*, respectively. Different approaches were tested to improve the simulations in this region, including the addition of coverage dependency terms. The solution found was to add 15.44 kJ mol^{-1} to the activated complex energies of the most sensitive reactions of the rWGSR (R24 and R25), if the feed ratio of CO_2/CO_X is higher than 0.65 (see Table 2). With this procedure, the model remains thermodynamically consistent.

This journal is © The Royal Society of Chemistry 2021

React. Chem. Eng., 2021, **6**, 868–887 | **877**

Table 2 Three-site field extended reaction mechanism for the methanol synthesis and the water-gas shift reaction over Cu (211) and Cu/Zn (211), thermodynamically consistent. (a): Cu (211), (b): Cu/Zn (211), (c): special Cu (211) site for hydrogen and water adsorption

No.	Reaction	Forward reaction			Reverse reaction		
		$\Delta S_f^{\neq} \times 10^3$ [kJ mol^{-1} K^{-1}]	$E_{A,f}$ [kJ mol^{-1}]	β [−]	$\Delta S_r^{\neq} \times 10^3$ [kJ mol^{-1} K^{-1}]	$E_{A,r}$ [kJ mol^{-1}]	β [−]
R1	$H_{2(g)} + 2 \cdot (c) \rightleftharpoons 2 \cdot H_{(c)}$	−119.24	69.57	0.000	1.72	93.01	0.000
R2	$CO_{(g)} + (a) \rightleftharpoons CO_{(a)}$	−158.23	0.00	0.000	0.00	58.37	0.000
R3	$CO_{(g)} + (b) \rightleftharpoons CO_{(b)}$	−151.60	8.90	−0.119	−6.64	0.00	0.119
R4	$CO_{2(g)} + (a) \rightleftharpoons CO_{2(a)}$	−144.74	0.00	−0.129	−7.22	52.29	0.129
R5	$CO_{2(g)} + (b) \rightleftharpoons CO_{2(b)}$	−138.11	0.00	−0.249	−13.86	51.59	0.249
R6	$H_3CO_{(a)} + H_{(c)} \rightleftharpoons CH_3OH_{(g)} + (a) + (c)$	56.99	81.22	−0.547	−181.26	32.93	0.547
R7	$H_3CO_{(b)} + H_{(c)} \rightleftharpoons CH_3OH_{(g)} + (b) + (c)$	47.03	92.56	−0.368	−171.30	23.61	0.368
R8	$H_2O_{(g)} + (c) \rightleftharpoons H_2O_{(c)}$	−177.19	0.00	0.378	21.08	31.21	−0.378
R9	$H_2O_{(c)} + (c) \rightleftharpoons OH_{(c)} + H_{(c)}$	5.99	79.84	0.140	21.60	105.17	−0.140
R10	$CO_{(a)} + H_{(c)} \rightleftharpoons HCO_{(a)} + (c)$	25.38	84.62	−0.299	−21.90	20.55	0.299
R11	$HCO_{(a)} + H_{(c)} \rightleftharpoons H_2CO_{(a)} + (c)$	15.73	56.26	−0.299	−8.10	92.81	0.299
R12	$CO_{2(a)} + H_{(c)} \rightleftharpoons HCOO_{(a)} + (c)$	36.44	77.74	−0.249	8.72	109.64	0.249
R13	$CO_{2(b)} + H_{(c)} \rightleftharpoons HCOO_{(a)} + (c)$	43.07	60.24	−0.368	2.08	105.43	0.368
R14	$HCOO_{(a)} + H_{(c)} \rightleftharpoons HCOOH_{(a)} + (c)$	10.42	128.23	0.000	−153.70	29.81	0.000
R15	$HCOO_{(b)} + H_{(c)} \rightleftharpoons HCOOH_{(b)} + (c)$	10.42	136.53	0.000	−153.70	7.72	0.000
R16	$HCOOH_{(a)} + H_{(c)} \rightleftharpoons H_2COOH_{(a)} + (c)$	−150.42	46.89	0.000	−25.96	62.43	0.000
R17	$HCOOH_{(b)} + H_{(c)} \rightleftharpoons H_2COOH_{(b)} + (c)$	−150.42	1.54	0.000	−25.96	48.92	0.000
R18	$H_2COOH_{(a)} + (c) \rightleftharpoons H_2CO_{(a)} + OH_{(c)}$	−20.59	20.52	−0.249	−15.21	38.77	0.249
R19	$H_2COOH_{(b)} + (c) \rightleftharpoons H_2CO_{(b)} + OH_{(c)}$	−13.95	11.22	−0.368	−21.85	9.96	0.368
R20	$H_2CO_{(a)} + H_{(c)} \rightleftharpoons H_3CO_{(a)} + (c)$	42.42	52.66	−0.547	−13.47	107.12	0.547
R21	$H_2CO_{(b)} + H_{(c)} \rightleftharpoons H_3CO_{(b)} + (c)$	32.46	51.46	−0.368	−3.51	132.06	0.368
R22	$CO_{(a)} + OH_{(c)} \rightleftharpoons COOH_{(a)} + (c)$	−11.31	79.90	−0.119	−3.74	16.05	0.119
R23	$CO_{(b)} + OH_{(c)} \rightleftharpoons COOH_{(b)} + (c)$	−11.31	13.33	−0.119	−3.74	16.05	0.119
R24	$COOH_{(a)} + OH_{(c)} \rightleftharpoons CO_{2(a)} + H_2O_{(c)}$	9.92	17.09	−0.119	−22.36	60.82	0.119
R25	$COOH_{(b)} + OH_{(c)} \rightleftharpoons CO_{2(b)} + H_2O_{(c)}$	9.92	17.09	−0.119	−22.37	60.82	0.119
If the CO_2/CO_X ratio in feed is higher than 0.65, the activation energies of reactions 24 and 25 are adjusted:							
R24	$COOH_{(a)} + OH_{(c)} \rightleftharpoons CO_{2(a)} + H_2O_{(c)}$	9.92	**32.53**	−0.119	−22.36	**76.22**	0.119
R25	$COOH_{(b)} + OH_{(c)} \rightleftharpoons CO_{2(b)} + H_2O_{(c)}$	9.92	**32.53**	−0.119	−22.37	**76.22**	0.119

Table 3 Operating conditions of the considered database, which consists of different setups

Database	No. of points	Reactor	Pressure (bar)	Temperature (°C)	GHSV (L h^{-1} g$_{cat.}^{-1}$)	H$_2$ feed (% v/v)	CO feed (% v/v)	CO$_2$ feed (% v/v)	Inert feed (% v/v)	Conversion of CO$_X$ (%)
This work	359	PFR	40–60	210–260	24–40	35–60	3–30	0–20	20–50	0.9–30.9
Seidel	139	CSTR	30–70	230–260	3.6	60–76	0–21	0–13	15–16	2.9–52.8
Park[a]	98	PFR	50–90	230–340	8–40	50–83	7–29	2–16	0–28	5.1–56.0
Slotboom	94	PFR	20–50	178–260	1.3–6.5	66–80	0	12–25	0–11	0.4–9.6

[a] Only the experiments containing both CO and CO$_2$ in the feed were considered.

In Fig. 6, the normalized residues of the two-case model are shown for each carbon-containing species. The model quantitatively reproduces the 690 measurements, with the majority of the data points being inside the ±20% lines (58% of the methanol points and ≥90% of CO and CO$_2$ points). CO$_2$ simulation error is always smaller than 40%, and only 3.4% of CO data points and 17% of methanol data points are outside the ± 40% lines. The sum of the relative squared errors (χ^2), the mean error (ME$_j$) and the mean squared error of the predictions are calculated for CO (j = 1), CO$_2$ (j = 2), and methanol (j = 3), and are shown in Table 4.

$$\chi^2 = \sum_{j=1}^{3} \sum_{n=1}^{N_p} \left(\frac{y_{j,out}^n - \hat{y}_{j,out}^n}{y_{j,out}^n} \right)^2 \qquad (53)$$

$$ME_j = \frac{1}{N_p} \cdot \sum_{1}^{N_p} \left| \frac{y_{j,out}^n - \hat{y}_{j,out}^n}{y_{j,out}^n} \right| \qquad (54)$$

$$MSE_j = \frac{1}{N_p} \cdot \sum_{1}^{N_p} \left(\frac{y_{j,out}^n - \hat{y}_{j,out}^n}{y_{j,out}^n} \right)^2 \qquad (55)$$

Considering all experiments, the mean error (ME) values of CO, CO$_2$ and methanol concentration are 8.0, 3.3, and 21.7%, respectively. These values are even lower when looking only to mixed feeds (H$_2$/CO/CO$_2$). The mean squared errors (MSE) are also significantly low (see Table 4).

In Fig. 7, it is shown the experimental and simulated values of methanol output concentration for different conditions and setups. It can be seen that the simulations are significantly close to the experiments and the trends are

878 | *React. Chem. Eng.*, 2021, **6**, 868–887

This journal is © The Royal Society of Chemistry 2021
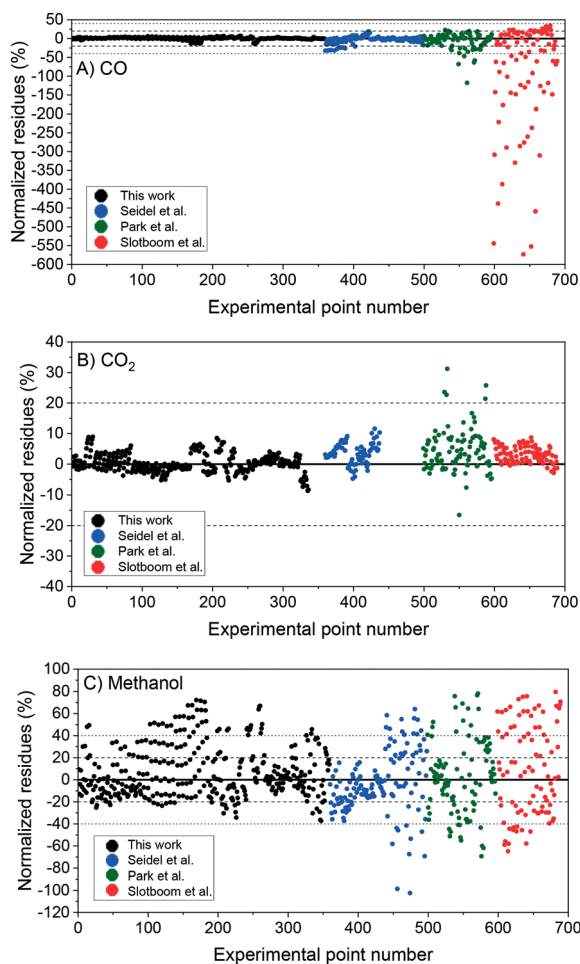
Fig. 5 Original model simulation: normalized residues of the simulation of the experiments from this work (1–359), from Seidel *et al.*[15] (360–498), from Park *et al.*[14] (499–596), and from Slotboom *et al.* (597–690).[16] A) Carbon monoxide. B) Carbon dioxide. C) Methanol.
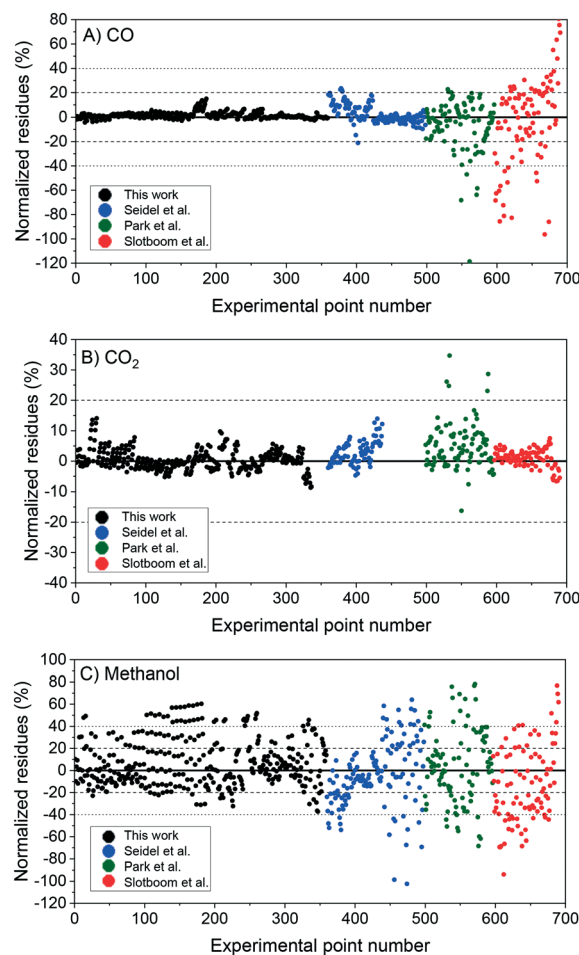
Fig. 6 Two-case model simulation: normalized residues of the simulation of the experiments from this work (1–359), from Seidel *et al.*[15] (360–498), from Park *et al.*[14] (499–596), and from Slotboom *et al.* (597–690).[16] A) Carbon monoxide. B) Carbon dioxide. C) Methanol.

adequately predicted. In Fig. 8, the error of the prediction of the carbon-containing compounds is shown as a function of $\bar{y}_{CO_2,0}$ (*x*-axis) and temperature (*y*-axis) for our experiments at the operating conditions of 40 bar, 24 L h^{-1} g$_{cat}^{-1}$ and H$_2$/CO$_x$/N$_2$ $\approx$ 45.3/14.3/40.4% v/v. The model simulates CO and CO$_2$ accurately for the entire studied region. The simulation of methanol is also reasonable, with slight underestimations at high temperatures and low $\bar{y}_{CO_2,0}$, and moderate underestimations at low temperatures and high $\bar{y}_{CO_2,0}$. This leads to the conclusion that there is some positive effect on CO$_2$ hydrogenation at low temperature when the concentration of CO$_2$ is increased, which is not reflected in this model. This effect is shown in both our own experiments and experiments from literature.[51] Still, the model adequately simulates this region (low temperature and high $\bar{y}_{CO_2,0}$) for lower values of GHSV is lower (which means higher conversion). This is demonstrated in the simulation of the experiments from Slotboom *et al.*[16] which have no CO in feed ($\bar{y}_{CO_2,0}$ = 1) and are reasonably reproduced.

4.2 Reaction flow and sensitivity analysis

The validated model was used to simulate the methanol synthesis at an extended range of conditions. In Fig. 9, it is shown the turnover frequency of the different reaction paths and the CO$_X$ conversion along the reactor. The operating conditions are 60 bar, 220 °C, 4.8 L$_S$ h^{-1} g$_{cat}^{-1}$, and a feed concentration of H$_2$/CO$_x$ = 80/20% v/v. Fig. 9 is complemented by the coverages of the surface species (Fig. 10) and the zinc coverage along the reactor (Fig. 11). In Fig. S6–S8† analogous diagrams are shown for an operating temperature of 250 °C.

According to the simulations, CO hydrogenation on site a (Cu) is only relevant at CO-rich feeds (*e.g.* 20% of the methanol production at $\bar{y}_{CO_2,0}$ = 0.25), CO$_2$ hydrogenation on site a (Cu) does not occur significantly at any condition, and CO$_2$ hydrogenation on site b (Cu/Zn) is the main reaction path for the production of methanol, in agreement with findings from DFT studies.[24,30]

At CO-rich conditions (*e.g.* $\bar{y}_{CO_2,0}$ ≤ 0.50), CO$_2$ conversion and (consequently) water generation are fast within the initial

This journal is © The Royal Society of Chemistry 2021

React. Chem. Eng., 2021, **6**, 868–887 | 879

Table 4 Statistical indicators of the model performance in predicting the carbon-containing compounds

Feed		$H_2/CO/CO_2$			H_2/CO		H_2/CO_2		
Data		This work	Seidel *et al.*	Park *et al.*	This work	Seidel *et al.*	Seidel *et al.*	Slotboom *et al.*	All
N° of points		324	46	98	35	61	32	94	690
χ^2		17.01	0.81	16.86	2.29	9.32	3.35	25.10	74.74
CO	ME	0.0215	0.0528	0.1424	0.0104	0.0265	0.1214	0.2776	0.0802
	MSE	0.0010	0.0055	0.0488	0.0002	0.0012	0.0171	0.1314	0.0266
CO_2	ME	0.0240	0.0444	0.0629			0.0261	0.0263	0.0325
	MSE	0.0011	0.0032	0.0081			0.0011	0.0010	0.0024
CH_3OH	ME	0.1688	0.0834	0.2704	0.2228	0.3212	0.2582	0.3104	0.2172
	MSE	0.0504	0.0089	0.1151	0.0651	0.1515	0.0804	0.1347	0.0794

10 cm of the reactor, mainly due to CO_2 hydrogenation, but probably also due to contributing rWGSR (depending on the CO_2/CO_x ratio and the temperature). Furthermore, the WGSR rate increases rapidly along the reactor, and after a certain amount of water has been produced (it is dependent on the operating conditions), the WGSR rate is the approximately equal to the CO_2 hydrogenation rate. From this axial position on (*ca.* 10 cm, Fig. 9A and B), CO_2 concentration remains constant, because it is consumed in the CO_2 hydrogenation but regenerated in the WGSR. Therefore, from this axial position on, only CO is converted, through the combination of WGSR and CO_2 hydrogenation and through direct CO hydrogenation.

Fig. 7 Experimental and simulated values of methanol output concentration at different conditions. Databases: A) this work. B) Seidel *et al.*[15]

With more CO_2 content in the feed (*e.g.* $\bar{y}_{CO_2,0} \geq 0.75$), a higher conversion of CO_2 is achieved, which implies that higher amounts of water are generated, and the methanol synthesis is severely slowed down. At CO_2-rich feeds, there is significant CO production *via* the rWGSR, increasing with temperature (see Fig. S7†).
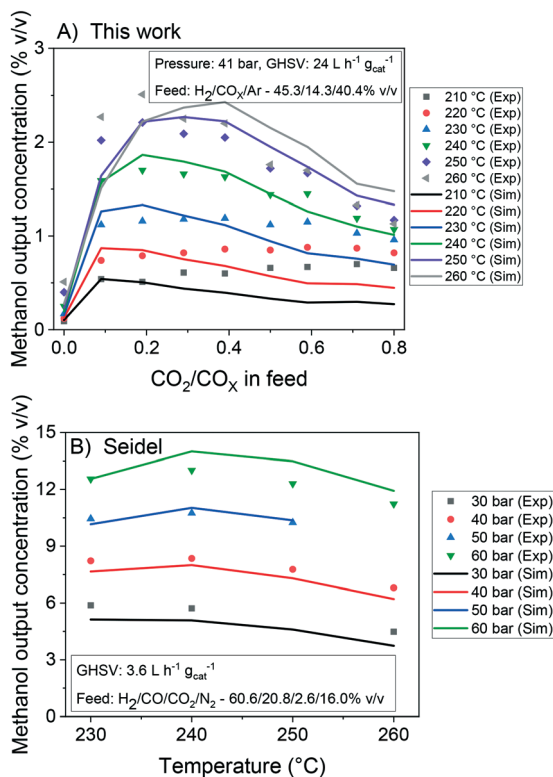
At constant temperature and pressure, the decrease of CO_2 hydrogenation rate on Cu/Zn, along the reactor length, has three main causes:

• The decrease of $H_{(c)}$ coverage, which is caused by $H_{2(g)}$ consumption;

• The zinc coverage (ϕ_{Zn}) decrease, caused by the generation of water and consumption of H_2 and CO,[27,29] which significantly changes the gas reducing power (eqn (32)).

• The product inhibition with the increase of $H_3CO_{(b)}$ and $OH_{(b)}$, because of methanol and water accumulation, respectively.

From our simulations, the product inhibition has the highest effect in reducing the reaction rate. This is particularly relevant for CO_2-rich feeds, in which a significant water accumulation takes place and, thus, $OH_{(c)}$ reduces the amount of free sites (c), as shown in Fig. 10C and D.

In a recent work,[52] a methanol-assisted autocatalytic mechanism was proposed, with water as the only effective inhibitor of the methanol synthesis. If appropriate DFT calculations were accessible, our model could be extended accordingly and this possibility could be investigated further.

In Fig. 12, the positive effects of pressure and CO_2 concentration, and the negative effect of temperature on formate coverage on Cu and on Cu/Zn are shown. Formate requires lower temperature, higher pressure, and higher CO_2 concentration to block the majority of Cu sites (Fig. 12A and B), but it covers most of the Cu/Zn sites even at mild conditions (Fig. 12C and D). Therefore, moderate consumption of CO_2 changes the formate coverage on Cu/Zn only slightly, and therefore the reaction rate of CO_2 hydrogenation is not as much affected by CO_2 consumption as by the factors previously discussed. This was experimentally demonstrated by varying the feed concentration of CO_2 while maintaining the other conditions constant, as shown in Fig. 13.

880 | *React. Chem. Eng.*, 2021, **6**, 868–887

This journal is © The Royal Society of Chemistry 2021
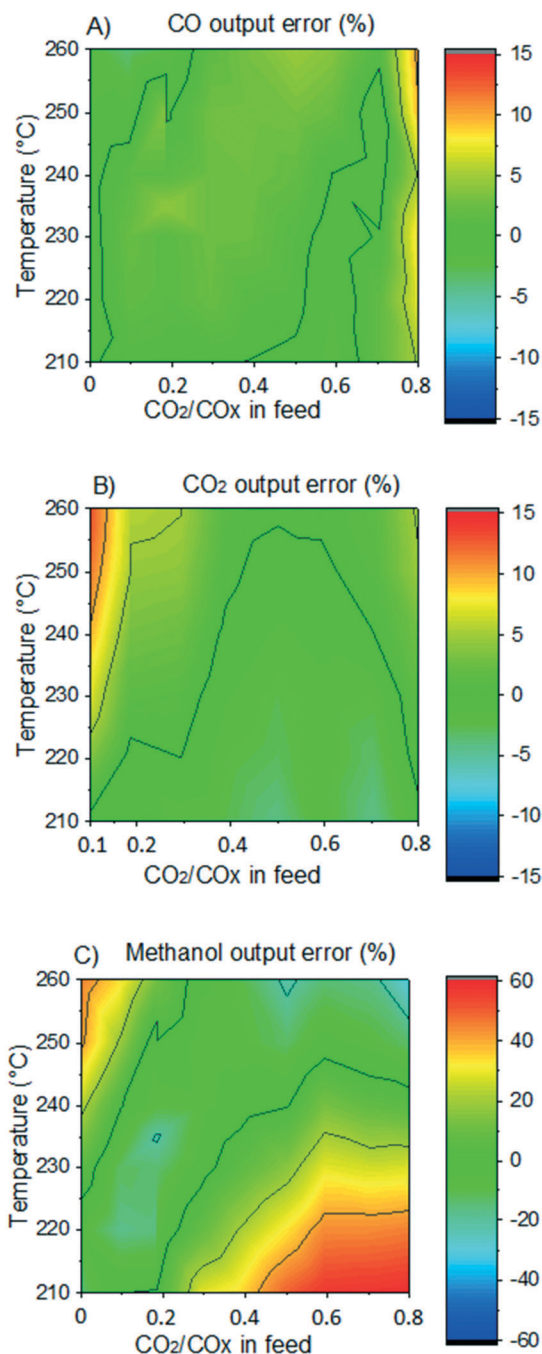
Fig. 8 Simulation error (color) as a function of CO_2/CO_x in feed and temperature. Operating conditions: 41 bar, GHSV = 24 L_S h^{-1} g$_{cat}$$^{-1}$, feed concentration: $H_2/CO_x/N_2$ = 45.3/14.3/40.4% v/v. A) CO. B) CO_2. C) Methanol.

the gas (Fig. 15), which includes the sensitivity of both CO and methanol generation. The DRC was also applied to a
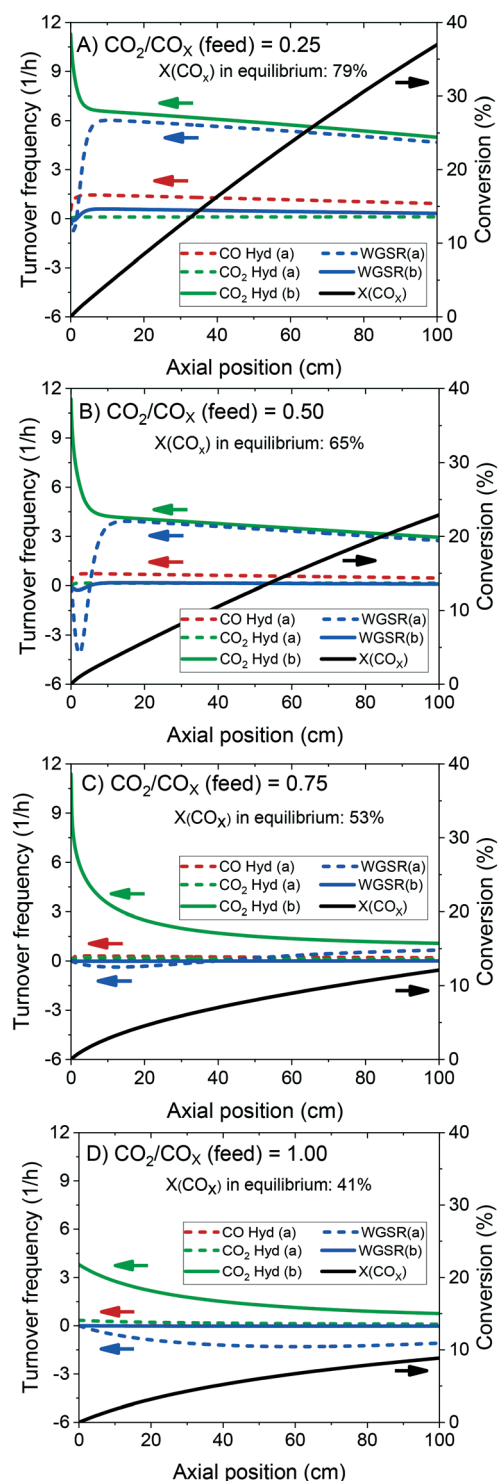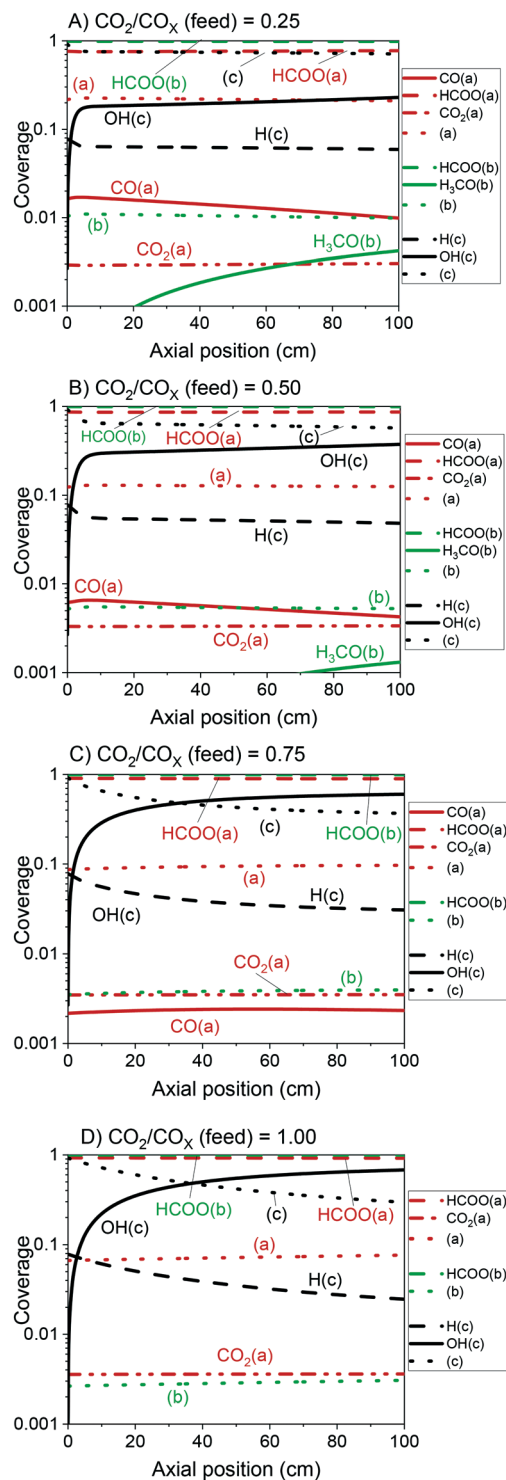

Fig. 9 Turnover frequency and conversion of CO_X (X) along a methanol synthesis reactor with a length of 100 cm, simulated with the kinetic model. The arrows show to which y-axis the curves belong. Operating conditions: 220 °C, 60 bar, GHSV = 4.8 L_S h^{-1} g$_{cat}$$^{-1}$, feed concentration: H_2/CO_x = 80/20% v/v. A) CO_2/CO_x = 0.25. B) CO_2/CO_x = 0.50. C) CO_2/CO_x = 0.75. D) CO_2/CO_x = 1.00.

The method of degree of rate control (DRC) is applied to investigate the sensitivity of the methanol production in relation to the free Gibbs energy of each surface intermediate and of each transition state of the reversible reactions. This analysis is shown at 60 bar (Fig. 14) and different temperatures considering a gas phase concentration at low conversion: $H_2/CO_x/CH_3OH/H_2O$ = 79.8/19.8/0.2/0.2% v/v. A separate analysis is made for the case of little CO content in

This journal is © The Royal Society of Chemistry 2021
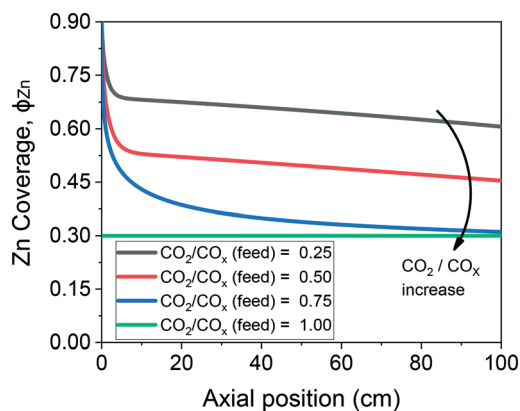
React. Chem. Eng., 2021, 6, 868–887 | 881

Fig. 10 Coverage of the surface species along the reactor with a length of 100 cm. Operating conditions: 220 °C, 60 bar, GHSV = 4.8 L_S h^{-1} g_{cat}^{-1}, feed concentration: H_2/CO_x = 80/20% v/v. A) CO_2/CO_x = 0.25. B) CO_2/CO_x = 0.50. C) CO_2/CO_x = 0.75. D) CO_2/CO_x = 1.00.

Fig. 11 Zinc coverage along the methanol synthesis reactor with a length of 100 cm. Operating conditions: 220 °C, 60 bar, GHSV = 4.8 L_S h^{-1} g_{cat}^{-1}, feed concentration: H_2/CO_x = 80/20% v/v.

Cu/Zn (R17, Table 2) for the entire operating region under study, which is in agreement with other DFT-derived models[19,53] and lumped kinetic models.[11,16] Xu et al.[22] concluded that the hydrogenation of formic acid is the RDS for the CO_2 hydrogenation at lower formate coverages, and the H_2COOH* association (R19, Table 2) is the RDS for high formate coverages, the latter conclusion being a result of the one-site approach made by the authors (see section 3.1). Grabow et al.[18] and Park et al.[21] found the hydrogenation of H_2CO* to be the RDS on Cu (111) without considering the zinc influence. Finally, the model presented here shows that the hydrogenation of formate (R15), a typically assumed RDS in formal kinetic models,[12,15] has a reasonable sensitivity in our model (0.20–0.35), but still far behind the sensitivity of R17 (0.50–0.70).
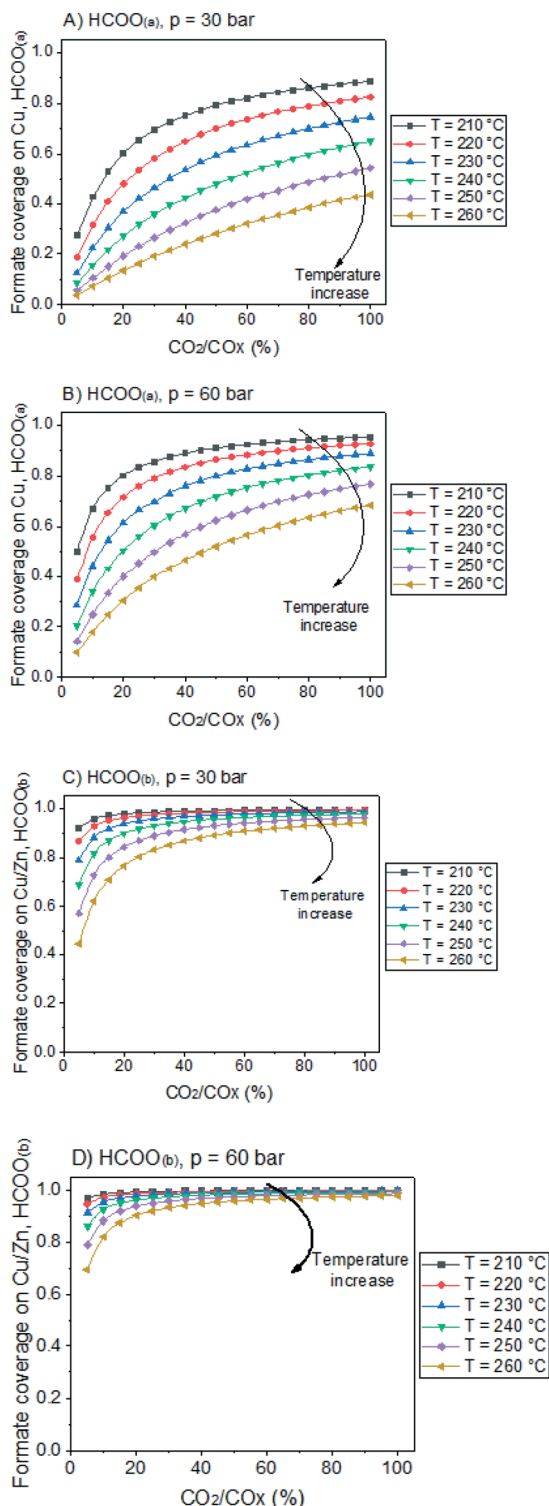
In the CO hydrogenation on Cu, the most sensible reaction of this microkinetic model is the hydrogenation of $HCO_{(a)}$ (R11), which is in agreement with findings of Van Rensburg et al.[19] In formal kinetic modeling studies, Graaf et al.[11] proposed the hydrogenation of H_2CO* (R20) to be the RDS, while Seidel et al.[15] assumed that the RDS is the hydrogenation of H_3CO* (R6).

From our DRC analysis of CO generation sensitivity at CO_2/CO_x = 0.987 (Fig. 15), the reaction between CO_2* and H_2O* on Cu (R24) is the RDS of the rWGSR. Other reported models that include the WGSR usually consider the redox mechanism[12,15] or the carboxyl mechanism without water assistance[16] to be the RDS, which have been tested here with DFT data and also evaluated elsewhere as not significant if compared to the water-assisted carboxyl mechanism.[31]

Regarding the participating intermediates, our findings suggest that formate on Cu/Zn ($HCOO_{(b)}$) is the most sensitive species, as it is the most abundant species, and participates on the second most sensitive reaction (formate hydrogenation), which produces the formic acid ($HCOOH_{(b)}$).

The rWGSR is mostly sensitive to formate adsorbed on Cu, although formate itself is a spectator of this reaction path, suggesting that formate may inhibit the rWGSR at a certain level. This hypothesis is further supported by the argument

pressure of 30 bar, and similar results to the ones at 60 bar were found (see Fig. S9 and S10†).

The most sensitive reaction according to our microkinetic model is the hydrogenation of formic acid ($HCOOH_{(b)}$) on

Fig. 12 Formate coverage on Cu and Cu/Zn active surfaces, as a function of CO_2/CO_x ratio in the gas phase. The gas phase concentration correspond to a typical low conversion condition: $H_2/CO_x/CH_3OH/H_2O$ = 79.8/19.8/0.2/0.2% v/v. The curves correspond to different temperatures. A) $HCOO_{(a)}$, 30 bar. B) $HCOO_{(a)}$, 60 bar. C) $HCOO_{(b)}$, 30 bar. D) $HCOO_{(b)}$, 60 bar.

that the rWGSR is much slower on Cu/Zn, which has a formate coverage close to 1.
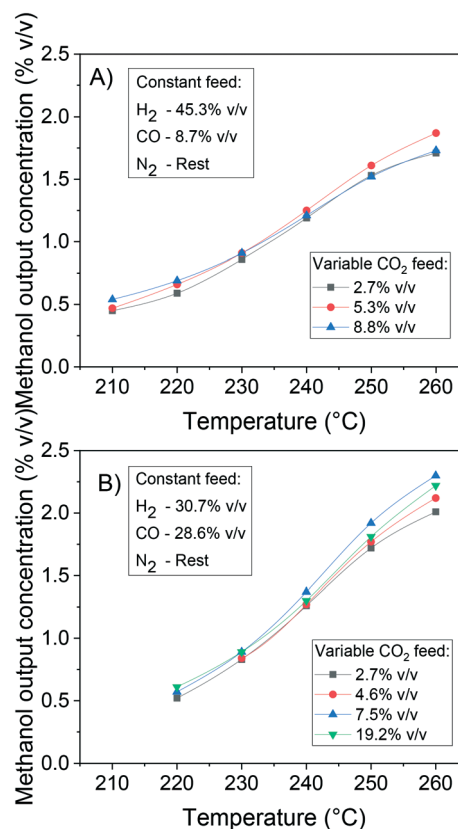
Fig. 13 Effect of CO_2 feed concentration on the methanol production at 41 bar, 220–260 °C and 32 L_S h^{-1} g_{cat}^{-1}. A) Constant feed H_2/CO = 45.3/8.7% v/v. B) Constant feed H_2/CO = 30.7/28.6% v/v.
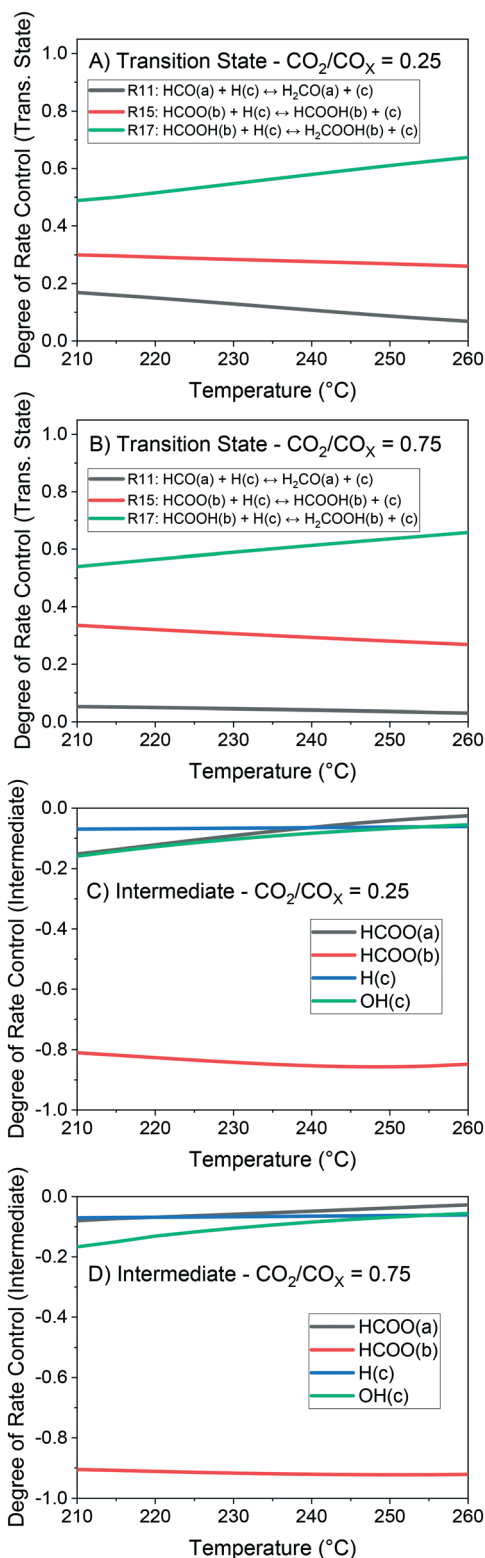
Summary and conclusions

A thermodynamically consistent microkinetic model was successfully developed, based on first principles DFT derived kinetic data for the methanol synthesis and the WGSR on Cu (211) and Cu/Zn (211). A method for the quantification of the zinc coverage dependent on the operating conditions, proposed in the literature, is applied here, and is slightly modified to improve the estimation for gas compositions rich in H_2 and CO.

With an extensive validation consisting in 359 own experiments (available in the ESI†) and experiments from three different sources in literature (*i.e.* 139 data points from Seidel *et al.*,[15] 98 data points from Park *et al.*,[14] and 94 data points from Slotboom *et al.*[16]), the model reproduces the system quantitatively in a broad range of relevant conditions, showing discrepancies only for the combination of low temperature, high CO_2/CO_x concentration in feed and high GHSV. The proposed model is based on theoretical calculations, and we believe it has a high change of accurately predicting the methanol synthesis outside the validation region.

The reaction flow analysis showed that methanol is mainly formed from CO_2 hydrogenation on site b (Cu/Zn), and that CO conversion is mostly due to the WGSR on site a (Cu). At CO-rich conditions, direct CO hydrogenation is responsible

This journal is © The Royal Society of Chemistry 2021

React. Chem. Eng., 2021, **6**, 868–887 | **883**

Fig. 14 Degree of rate control (DRC) analysis of the methanol production at 60 bar and 210–260 °C. Gas concentration: $H_2/CO_x/CH_3OH/H_2O$ = 79.8/19.8/0.2/0.2% v/v. A) Trans. state – CO_2/CO_x = 0.25. B) Trans. state – CO_2/CO_x = 0.75. C) Intermediate – CO_2/CO_x = 0.25. D) Intermediate – CO_2/CO_x = 0.75.
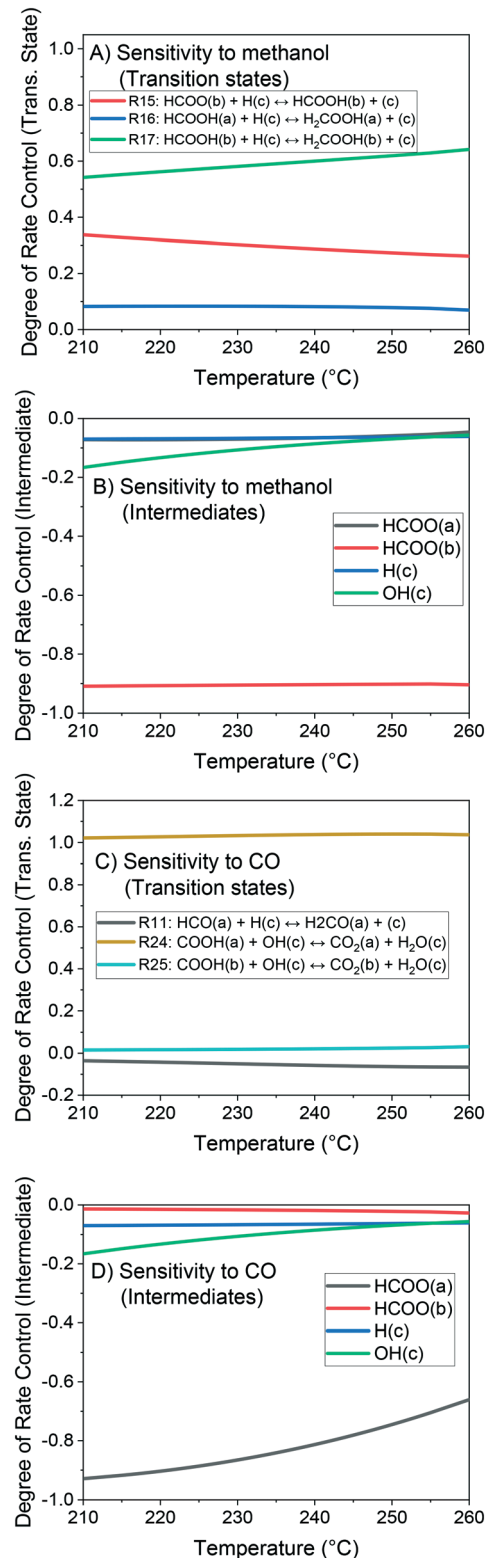
Fig. 15 Degree of rate control (DRC) analysis at 210–260 °C, 60 bar, and a gas concentration of $H_2/CO/CO_2/CH_3OH/H_2O$ = 79.8/0.2/19.6/0.2/0.2% v/v. A) Sensitivity to methanol, transition states. B) Sensitivity to methanol, intermediates. C) Sensitivity to CO, transition states. D) Sensitivity to CO, intermediates.

for some of the methanol generation (*e.g.* 20% of the methanol production for $CO_2/CO_X = 0.25$). On the other hand, this reaction pathway is strongly inhibited by formate accumulation on Cu surface at higher CO_2 concentrations.

The model suggests that formation of methanol and water leads to an accumulation of $H_3CO_{(b)}$ and $OH_{(c)}$, respectively, with both slowing down the overall reaction. This is particularly significant in the case of CO_2-rich feeds, as high amounts of water are generated in the process. We assume that the productivity should be increased by using reactor designs that enable product extraction *in situ*, such as using membranes, or integrating reaction and product condensation steps. This is especially encouraged for the conversion of CO_2 to methanol.

The sensitivity analysis, using the method of the degree of rate control (DRC), pointed out that the formic acid hydrogenation on site b (Cu/Zn) ($HCOOH_{(b)}$) is the most sensitive step (DRC around 0.60). Formate ($HCOO_{(a)}$) was found to be the most sensitive intermediate in the rWGSR, although it does not participate in this reaction, which suggests that the rWGSR is slowed down due to formate blocking of free sites. With this finding and based on the premise that formate only reacts further to produce methanol, we formulate the following hypothesis: If a modification on the Cu/Zn-based catalysts is realized, in which formate binds stronger on the Cu site and achieves coverages closer to 1, the rWGSR might be more effectively inhibited, and CO_2 conversion at CO_2-rich systems should be enhanced.

The presented microkinetic model can be further extended with additional reactions paths if DFT calculations are available (*e.g.* methanol dehydration to DME or methanol-assisted autocatalytic reaction paths).

The quantification of the zinc coverage may be improved by an approach on a higher level of theory for the zinc oxide activity, by an operando analysis to check which is the maximum zinc coverage on the surface at a H_2/CO feed, and with an approach for non-equilibrated WGSR and domination of zinc reduction *via* hydrogen (*e.g.* for high CO_2/CO_X ratio in feed).

Nomenclature

A_{Cat}	Active surface area (m^2)
$A_{n,m}$	Coefficient n of the Gibbs term of reaction path m (eqn (19))
$a_{n,j}$	Coefficient n of the Gibbs term of gas species j (eqn (14))
a_j	Activity of gas component j
$\Delta c_{p,m}$	Heat capacity change of global reaction m (kJ mol^{-1} K^{-1})
d_i	Crystallite diameter of species i (m)
DRC_i	Degree of rate control of a transition state or surface intermediate i
$E_{A,k}$	Activation energy of reaction k (kJ mol^{-1})
f_j	Fugacity of gas component j (Pa)

$G_j^0(T)$	Free Gibbs energy at 1 bar and temperature T (kJ mol^{-1})
$\Delta G_R^0(T)$	Free Gibbs energy of (global/surface) reaction R at 1 bar and temperature T (kJ mol^{-1})
$\Delta H_{298.15K}^0$	Standard reaction enthalpy (kJ mol^{-1})
ΔH_{seg}^0	Segregation enthalpy at 1 bar (kJ mol^{-1}) (see eqn (33) and (34))
h	Planck constant (6.62607×10^{-34} J s)
K_R	Equilibrium constant of reversible reaction R
k_b	Boltzmann constant (1.38065×10^{-23} J K^{-1})
L	Catalyst bed length (m)
M_i	Molar mass of species i (kg mol^{-1})
m_{Cat}	Catalyst mass (kg)
N_g	Number of gas components (—)
N_r	Number of surface reactions (—)
N_s	Number of surface intermediates (—)
$n_{M,Cat}$	Specific catalyst site quantity (mol kg^{-1})
$\dot{n}$	Total mole flow (mol s^{-1})
p_0	Reference pressure (1×10^5 Pa)
$q_{n,m}$	Thermodynamic constraint n of reaction pathway m
R	Universal gas constant (8.31446×10^{-3} kJ mol^{-1} K^{-1})
r_k	Turnover rate of reversible reaction k (s^{-1})
$\Delta S_k^{\neq}$	Entropy barrier of reaction k (kJ mol^{-1} K^{-1})
$\dot{s}_k$	Rate of reaction k (mol m^{-2} s^{-1})
T	Temperature (K)
w_k	Selectable weight of reaction k (—)
y_j	Mole fraction of gas component j (mol/mol)
$y_{j,out}^n$	Experimental value (point n) of mole fraction of gas component j of point n in the reactor outlet (mol/mol)
$\hat{y}_{j,out}^n$	Simulated value (point n) of mole fraction of gas component j of point n in the reactor outlet (mol/mol)
X_{Zn}	Solubility of zinc in the copper bulk (mol/mol)

Greek

α	Proposed linear relation parameter between the zinc oxide activity and the zinc solubility in the Cu bulk (—)
β_k	Correction term of reaction k because of the thermodynamic consistency (—)
Γ	Surface site density (mol m^{-2})
δ	Step size of the finite differences method (kJ mol^{-1})
γ_{Zn}	Activity coefficient of metallic zinc (—)
$\bar{\gamma}_i$	Surface energy of species i (kJ m^{-2})
$\xi_{k,m}$	Stoichiometric coefficient of a reversible surface reaction k in the global reaction pathway m
θ_i	Surface coverage of species i (—)
ρ_i	Density of species i (kg m^3)
σ_i	Number of surface sites occupied by species i (—)
v'_{ik}	Stoichiometric coefficient of reactant i in reaction k (—)
v''_{ik}	Stoichiometric coefficient of product i in reaction k (—)

ν_{ik}	Stoichiometric gain of species i in reaction k (—)
ϕ_i	Fraction of the site type of surface species i in relation to the total number of sites for carbon-containing compounds (sites a and b)
χ_i	Species i

Subscription

3p	Related to the three-parameter Gibbs function (eqn (19))
7p	Related to the seven-parameter Gibbs function (eqn (14))
DFT	Values from DFT calculations
in	Species entering the reactor
m	Reaction path number (see Fig. 2)
out	Species leaving the reactor

Superscription

+	Related to the forward reaction
−	Related to the reverse reaction
Orig.	Original DFT value from Studt *et al.*[30,31]
TC	Thermodynamically consistent value

Conflicts of interest

There are no conflicts to declare.

Acknowledgements

References

1 N. Dahmen, E. Henrich, E. Dinjus and F. Weirich, *Energy Sustain. Soc.*, 2012, **2**, 3.

2 J.-K. Lee, I.-B. Lee and J. Han, *J. Ind. Eng. Chem.*, 2019, **75**, 77–85.

3 J. R. Rostrup-Nielsen, *Catal. Today*, 2000, **63**, 159–164.

4 P. Lv, Z. Yuan, C. Wu, L. Ma, Y. Chen and N. Tsubaki, *Energy Convers. Manage.*, 2007, **48**, 1132–1139.

5 N. Dahmen, U. Arnold, N. Djordjevic, T. Henrich, T. Kolb, H. Leibold and J. Sauer, *J. Supercrit. Fluids*, 2015, **96**, 124–132.

6 M. Kopp, D. Coleman, C. Stiller, K. Scheffer, J. Aichinger and B. Scheppat, *Int. J. Hydrogen Energy*, 2017, **42**, 13311–13320.

7 G. A. Olah, A. Goeppert and G. K. S. Prakash, *J. Org. Chem.*, 2009, **74**, 487–498.

8 J. Artz, T. E. Müller, K. Thenert, J. Kleinekorte, R. Meys, A. Sternberg, A. Bardow and W. Leitner, *Chem. Rev.*, 2018, **118**, 434–504.

9 J. B. Hansen and P. E. H. Nielsen, in *Handbook of Heterogeneous Catalysis*, ed. E. H. G. Knözinger, F. Schüth and J. Weitkamp, 2nd edn, 2008, pp. 2920–2949, DOI: 10.1002/9783527610044.hetcat0148.

10 *Flaticon Icons*, Freepik, https://www.flaticon.com/authors/freepik, (accessed August/2020).

11 G. H. Graaf, E. J. Stamhuis and A. A. C. M. Beenackers, *Chem. Eng. Sci.*, 1988, **43**, 3185–3195.

12 K. M. V. Bussche and G. F. Froment, *J. Catal.*, 1996, **161**, 1–10.

13 C. V. Ovesen, B. S. Clausen, J. Schiøtz, P. Stoltze, H. Topsøe and J. K. Nørskov, *J. Catal.*, 1997, **168**, 133–142.

14 N. Park, M.-J. Park, Y.-J. Lee, K.-S. Ha and K.-W. Jun, *Fuel Process. Technol.*, 2014, **125**, 139–147.

15 C. Seidel, A. Jörke, B. Vollbrecht, A. Seidel-Morgenstern and A. Kienle, *Chem. Eng. Sci.*, 2018, **175**, 130–138.

16 Y. Slotboom, M. J. Bos, J. Pieper, V. Vrieswijk, B. Likozar, S. R. A. Kersten and D. W. F. Brilman, *Chem. Eng. J.*, 2020, **389**, 124181.

17 L. P. de Oliveira, D. Hudebine, D. Guillaume and J. J. Verstraete, *Oil Gas Sci. Technol.*, 2016, **71**, 45.

18 L. C. Grabow and M. Mavrikakis, *ACS Catal.*, 2011, **1**, 365–384.

19 W. J. van Rensburg, M. A. Petersen, M. S. Datt, J.-A. van den Berg and P. van Helden, *Catal. Lett.*, 2015, **145**, 559–568.

20 Y.-M. Liu, J.-T. Liu, S.-Z. Liu, J. Li, Z.-H. Gao, Z.-J. Zuo and W. Huang, *J. CO2 Util.*, 2017, **20**, 59–65.

21 J. Park, J. Cho, Y. Lee, M.-J. Park and W. B. Lee, *Ind. Eng. Chem. Res.*, 2019, **58**, 8663–8673.

22 D. Xu, P. Wu and B. Yang, *J. Phys. Chem. C*, 2019, **123**, 8959–8966.

23 M. Huš, D. Kopač, N. S. Štefančič, D. L. Jurković, V. D. B. C. Dasireddy and B. Likozar, *Catal. Sci. Technol.*, 2017, **7**, 5900–5913.

24 M. Behrens, F. Studt, I. Kasatkin, S. Kühl, M. Hävecker, F. Abild-Pedersen, S. Zander, F. Girgsdies, P. Kurr, B.-L. Kniep, M. Tovar, R. W. Fischer, J. K. Nørskov and R. Schlögl, *Science*, 2012, **336**, 893–897.

25 F. Studt, F. Abild-Pedersen, J. B. Varley and J. K. Nørskov, *Catal. Lett.*, 2013, **143**, 71–73.

26 Y. Morikawa, K. Iwata, J. Nakamura, T. Fujitani and K. Terakura, *Chem. Phys. Lett.*, 1999, **304**, 91–97.

27 J. D. Grunwaldt, A. M. Molenbroek, N. Y. Topsøe, H. Topsøe and B. S. Clausen, *J. Catal.*, 2000, **194**, 452–460.

28 R. van den Berg, G. Prieto, G. Korpershoek, L. I. van der Wal, A. J. van Bunningen, S. Lægsgaard-Jørgensen, P. E. de Jongh and K. P. de Jong, *Nat. Commun.*, 2016, **7**, 13057.

29 S. Kuld, M. Thorhauge, H. Falsig, C. F. Elkjær, S. Helveg, I. Chorkendorff and J. Sehested, *Science*, 2016, **352**, 969–974.

30 F. Studt, M. Behrens, E. L. Kunkes, N. Thomas, S. Zander, A. Tarasov, J. Schumann, E. Frei, J. B. Varley, F. Abild-Pedersen, J. K. Nørskov and R. Schlögl, *ChemCatChem*, 2015, **7**, 1105–1111.

31 F. Studt, M. Behrens and F. Abild-Pedersen, *Catal. Lett.*, 2014, **144**, 1973–1977.

32 S. Polierer, J. Jelic, S. Pitter and F. Studt, *J. Phys. Chem. C*, 2019, **123**, 26904–26911.

33 B. Hammer, *Phys. Rev. B: Condens. Matter Mater. Phys.*, 2001, **63**, 205423.

34 A. B. Mhadeshwar, J. R. Kitchin, M. A. Barteau and D. G. Vlachos, *Catal. Lett.*, 2004, **96**, 13–22.

35 D.-Y. Peng and D. B. Robinson, *Ind. Eng. Chem. Fundam.*, 1976, **15**, 59–64.

36 L. Meng and Y.-Y. Duan, *Fluid Phase Equilib.*, 2005, **238**, 229–238.

37 L. Meng, Y.-Y. Duan and X.-D. Wang, *Fluid Phase Equilib.*, 2007, **260**, 354–358.

38 U. K. Deiters, *Fluid Phase Equilib.*, 2013, **352**, 93–96.

39 M. G. Evans and M. Polanyi, *Trans. Faraday Soc.*, 1935, **31**, 875–894.

40 H. Eyring, *J. Chem. Phys.*, 1935, **3**, 107–115.

41 H. Stotz, L. Maier, A. Boubnov, A. T. Gremminger, J. D. Grunwaldt and O. Deutschmann, *J. Catal.*, 2019, **370**, 152–175.

42 K. H. Delgado, L. Maier, S. Tischer, A. Zellner, H. Stotz and O. Deutschmann, *Catalysis*, 2015, **5**, 871–904.

43 E. Goos, A. Burcat and B. Ruscic, *New NASA thermodynamic polynomials database* http://garfield.chem.elte.hu/Burcat/ THERM.DAT Acess: Aug/2020.

44 R. Schlögl, *Angew. Chem., Int. Ed.*, 2015, **54**, 3465–3520.

45 B. L. D. O. Campos, A. O. S. D. Costa and E. F. D. Costa Junior, *Sol. Energy*, 2017, **157**, 321–327.

46 B. L. D. O. Campos, A. O. S. D. Costa, K. C. de Souza Figueiredo and E. F. D. Costa Junior, *Desalination*, 2018, **437**, 184–194.

47 R. C. Kohberger, *Anal. Biochem.*, 1980, **101**, 1–6.

48 B. Leite, T. Croguennec, A. Halabi and E. F. D. Costa Junior, *J. Food Eng.*, 2021, **292**, 110272.

49 C. Stegelmann, A. Andreasen and C. T. Campbell, *J. Am. Chem. Soc.*, 2009, **131**, 8077–8082.

50 C. T. Campbell, *ACS Catal.*, 2017, **7**, 2770–2779.

51 H. Ruland, H. Song, D. Laudenschleger, S. Stürmer, S. Schmidt, J. He, K. Kähler, M. Muhler and R. Schlögl, *ChemCatChem*, 2020, **12**, 3216–3222.

52 J. Thrane, S. Kuld, N. D. Nielsen, A. D. Jensen, J. Sehested and J. M. Christensen, *Angew. Chem., Int. Ed.*, 2020, **59**, 18189–18193.

53 M. S. Tameh, A. K. Dearden and C. Huang, *J. Phys. Chem. C*, 2018, **122**, 17942–17953.

This journal is © The Royal Society of Chemistry 2021

React. Chem. Eng., 2021, **6**, 868–887 | **887**